Experimental Investigations and Modeling of the Strain Sensing Response of Matrices Containing Metallic Inclusions

by

Swaptik Chowdhury

A Thesis Presented in Partial Fulfillment
of the Requirements for the Degree
Master of Science

Approved May 2017 by the
Graduate Supervisory Committee:

Narayanan Neithalath, Chair
Subramaniam Rajan
Christian G. Hoover

ARIZONA STATE UNIVERSITY

August 2017

ABSTRACT

This study explores the possibility of two matrices containing metallic particulates to act as smart materials by sensing of strain due to the presence of the conducting particles in the matrix. The first matrix is a regular Portland cement-based one while the second is a novel iron-based, carbonated binder developed at ASU. Four different iron replacement percentages by volume (10%, 20%, 30% and 40%) in a Portland cement matrix were selected, whereas the best performing iron carbonate matrix developed was used. Electrical impedance spectroscopy was used to obtain the characteristic Nyquist plot before and after application of flexural load. Electrical circuit models were used to extract the changes in electrical properties under application of load. Strain sensing behavior was evaluated with respect to application of different stress levels and varying replacement levels of the inclusion. A similar approach was used to study the strain sensing capabilities of novel iron carbonate binder. It was observed that the strain sensing efficiency increased with increasing iron percentage and the resistivity increased with increase in load (or applied stress) for both the matrices. It is also found that the iron carbonate binder is more efficient in strain sensing as it had a higher gage factor when compared to the OPC matrix containing metallic inclusions.

Analytical equations (Maxwell) were used to extract frequency dependent electrical conductivity and permittivity of the cement paste (or the host matrix), interface, inclusion (iron) and voids to develop a generic electro-mechanical coupling model to for the strain sensing behavior. COMSOL Multiphysics 5.2a was used as finite element analysis software to develop the model. A MATLAB formulation was used to generate the microstructure with different volume fractions of inclusions. Material properties were

assigned (the frequency dependent electrical parameters) and the coupled structural and electrical physics interface in COMSOL was used to model the strain sensing response. The experimental change in resistance matched well with the simulated values, indicating the applicability of the model to predict the strain sensing response of particulate composite systems.

DEDICATION

This thesis is dedicated to my parents who have taken innumerable sacrifices in every stage of their life and have provided me with guidance and support throughout my academic career. Without their love, affection, support and unwavering belief in me, this work would not have reached its conclusion.

ACKNOWLEDGMENTS

First and foremost, I would like to express my heartfelt gratitude and regards to my advisor Dr. Narayanan Neithalath to provide me an opportunity to work in his research group. I am grateful for his valuable lessons on the fundamentals of properties of concrete and damage detection. He has guided me through my tough academic decisions and has shown me the importance of attending to details which performing experiments and simulations alike. I am eternally gratified to him for his undivided attention, encouragement and motivation throughout my research.

I would like to extend my regards to my committee members: Dr. Subramaniam D. Rajan and Dr. Christian G. Hoover for serving in my committee and their guidance throughout my study. I would like to thank my colleagues Naman, Pu, Dr. Akash, Aashay, Matt, Madhur and Dr. Sumanta for supporting and helping me during the experimental phase and during simulations.

I greatly appreciate the assistance provided by lab support team and engineering technical services comprising of Jeff Long and Peter Goguen for all their assistance during my study

TABLE OF CONTENTS

Page

CHAPTER Page

LIST OF TABLES

Table Page

LIST OF FIGURES

Figure Page

Figure Page

Figure Page

Chapter 1: Introduction and Literature Review

1.1 Background

The Current state of Infrastructure: The huge infrastructural boom in the late 20th century led to the use of large amounts of concrete in bridges, roads and high-rise building and most of these infrastructures are in dire need of repair and rehabilitation now. In the 2017 ASCE infrastructural report card, they gave a grade of D+ to the overall US infrastructure. ASCE observed significant levels of deterioration for dams, bridges and roads that were subjected to increased usage, which exceeded the initial demand for which they were constructed. They also analyzed that approximately $ 2.0 trillion would be required to repair or replace all the aging infrastructure of the United States and projection shows that 3.5% of the GDP will be needed by 2025 to improve and reinvigorate the existing infrastructure[1]. The aging infrastructure also causes other issues such as reduced capacity which increases congestion and thus causing loss in productivity and wasted fuel. ASCE also observed that many structural entities have become structurally deficient (9.1% of bridges were structurally deficient in 2016), and with each passing day many of our critical structures are approaching end of their design life. The other disadvantages of poor infrastructure includes health hazards such as the pipeline burst in Harlem (2014), human injuries and fatality due to collapsing aging bridges and residential projects, unhealthy conditions due to frustrating commute causing decrease in productivity, and environmental degradation due to congestion.

Thus, assessing, repairing and rehabilitating the existing structure have attracted immense focus. Rather than investing in the expensive repairs after the structure has lost its serviceability, it would be wiser economically to take proactive measures by monitoring

the critical structures regularly and employing remedial measures if need arises. Nondestructive test (NDT) is one of the more proactive and economical means which allows monitoring the structures regularly and help to predict performance without being invasive [2]. NDT is useful for both new and old structures and it is very useful in quality control, determining the location of damage, monitoring long term changes associated with deterioration caused by over loading, fatigue, corrosion, environmental degradation.

Novel structural concretes: In last few decades, novel composite materials with specifically targeted mechanical and durability properties have been developed. Composite materials with properties such as light weight, high stiffness and flexibility, better durability characteristics (shrinkage, thermal, chloride permeability, corrosion etc.), high yield strength and better fracture properties have been developed for application in aerospace, construction materials, and semiconductor industries. A composite material usually comprises of a reinforcement phase in a matrix phase. The reinforcement can be in the form of random short fibers, continuous long fibers, or particulates/fillers [3]–[5]. One of the oldest and most versatile composite materials is concrete which has been used for centuries as a preferred construction material.

The use of random short metallic fibers in concrete has been known to enhance compressive and flexural strengths, fracture toughness and tensile ductility, and reduces drying shrinkage. The randomly distributed fibers facilitate crack bridging and thereby provide ductility (or fiber increases the strain capacity at peak load and provides energy absorption in the post-peak portion thus preventing a catastrophic brittle failure). One of the more exciting avenues of metallic reinforcement use in cementitious composite is to

sense strain or damage using the characteristic electrical property of the composite, which is the focus of this thesis.

Sensing methods for concrete structures: Generally, external sensors are employed to collect and analyze the structure's response by utilizing the vibrational frequency of the structure. Many of the non-destructive evaluation (NDE) methods commonly used are based on active sensing in which a transducer introduces stress waves and then using the same transducer or another receiver to receive the wave after it has travelled through the sample. As the speed of the wave is a function of modulus of elasticity, Poisson's ratio, density and geometry of the solid, analyzing the waves received can help in determining the characteristics of the solid, which includes the presence of defects if any, their locations and other characteristics. Examples of such methods include pulse echo and pitch catch. The disadvantages associated with the stress wave methods are the wave attenuation over large distances and wave distribution due to the presence heterogeneities causing complex wave patterns.

Electrical impedance spectroscopy (EIS) employs changes in impedance of the sample to detect the presence of defects in concrete. The inclusion of conductive phases in concrete such as iron and steel fibers, carbon fibers, graphite powder, carbon nanofibers or nanotubes provide another avenue of nondestructive testing. Due to the inclusion of these fibers, the electrical resistivity of the cementitious composite is reduced and they render the composite 'smart' in a way that it provides an electrical response to a strain or stress stimulus. The response includes changes in resistivity or permittivity as a function of applied strain or stress. Such self-sensing is a preferred method as the whole composite is acting as a sensor and it can be used to detect a wide range of strains. Thus, metallic

particulate reinforced cementitious composites can be described as multifunctional composites where both enhanced mechanical properties and self-sensing are provided intrinsically by the material, rather than through external means.

The phenomenon of strain sensing in concrete has been studied mainly in carbon fiber reinforced cement composites [4], [6]–[8]. It is known through various studies that the reason for the change in electrical properties after the application of load is due to changes in the average position of fibers with respect to each other and with respect to matrix, and structural changes in the interface between fiber and the matrix. Thus, it is important to understand the microstructural change that influences the electrical response of the composite under load in order to develop economical composites with strain sensing capabilities. Numerical simulations of the microstructural response also helps better understand the effect of different factors such as shape and size of the inclusions, its volume fraction, distribution in the matrix, interface thickness and corresponding electrical properties, on the strain sensing or 'smart' behavior of these composites. Such an approach is adopted in this thesis.

1.2 Objectives

The major objectives of this thesis are as follows:

- Evaluating the applicability of waste iron powder (from steel shot blasting operations) as a particulate reinforcement in cementitious matrices for strain sensing;
- Exploring the use of iron carbonate binder developed at ASU as a self-sensing material for structural applications; and

- Development of a coupled electro-mechanical finite element formulation to model the strain sensing behavior of particulate reinforced cement composites.

1.3 Research Tasks:

The following research tasks were carried out to accomplish the above-stated objectives.

- Developing an experimental procedure for testing of strain sensing of composites using a standard three-point bending test and the influence of volume fraction of iron powder on electrical response;
- Analyzing the fractional change in resistance under stress and its changes that enable the functioning of these composites as strain sensing materials.
- Developing a microstructural model on which a finite element (FE)-based loosely coupled electro-mechanical model can be implemented;
- Establishing methodologies to determine the effective electrical and mechanical properties of the phases of the composite to be included in the FE model;
- Evaluating the influence of volume fraction and shape of iron powder among other parameters on the microstructural stress distribution and the electrical response (electrical conductivity and permittivity); and
- Predicting the strain sensing response through the numerical model, and establishing the utility of the loosely coupled model to act as a sensing material design tool (to obtain size, shape and volume fraction of particulates, interface properties.

1.4 Organization of Thesis

This section presents the overall organization of this thesis.

Chapter 2: This chapter details the development of experimental procedure for strain sensing which involves sample preparation, testing methods including the test setup for impedance spectroscopy, analysis of Nyquist plots, circuit model development and their limitations, percolation threshold and analysis of fractional change in resistivity ($\frac{\triangle(R)}{R0}$) to help establish the composite as a smart material.

Chapter 3: This chapter details the procedure adopted to extract the fundamental electrical properties to be used as inputs to the FE model. The methodology adopted to back-calculate the properties of phases for which experimental data was not available also forms part of this chapter. The influence of properties of phases and the shape of inclusions on the electrical response also is reported here.

Chapter 4: This chapter demonstrates the development of a multiphase microstructural model including the methodology to generate the microstructure, the considered boundary conditions, and the coupled electro-mechanical FE model which is generic to multi-phase composite materials.

Chapter 5: This chapter presents the conclusions and recommendations for future work.

1.5 Literature Review

An extensive literature review was conducted on different fibers that are used in 'smart' cementitious composites. The most common fibers used in the strain sensing are carbon and steel fibers. Existing literature on the novel iron carbonate binder is also summarized.

1.5.1 Carbon Fiber and Carbon Nanotube Reinforced Cementitious Composites

Shu et al (2015) [9] investigated the effect of carbon fiber on the mechanical properties of cementitious composites. They varied the fiber size from few micrometers to few

millimeters. They observed that the microfibers improve the pre peak load tensile efficiency of the composite when compared to macrofiber, but macrofiber satisfactorily improved the modulus of resilience and the toughness index. The fiber reinforced composite demonstrated improved energy absorption when compared to the control mixture. This established that fiber reinforcement improves the energy absorption before the critical crack formation. One issue in using macro fiber was the related to macro-fiber dispersion and it was concluded that fiber pullout was the reason of failure rather than fiber rupture. Similar results were reported by Xu et al. (2015) [10] who studied the effect of carbon nanotubes (CNTs) on the microstructure and the mechanical properties of the fiber-reinforced cement composite. They observed that the compressive and flexural strengths were greatly improved with increasing CNT volume fraction and reported debonding and crack bridging as major causes of the failure.

Chen and Chung (1995) [7] reported a new strain/stress sensor based on the change in electrical properties under tension and flexural loading. They used 0.5% of short carbon fibers by weight of cement, and for electrical measurement, DC current in the range of 0.1 A to 4 A was used. They observed little or no smart behavior or no strain sensing when no fiber or non-conducting fibers such as polyethylene was utilized. They argued that electrical response of concrete may show slight sensitivity to strain due to the presence of the pore fluid but conducting fibers greatly amplify the strain sensing behavior. They attributed the observed increase in conductivity under loading to the effects of slight pull-out or de-bonding. Smart behavior was also observed in concrete but the fractional change in resistance ($\Delta R/R_0$) was larger in mortar than in concrete because

the effectiveness of fibers in crack control was being hampered in the presence of coarse aggregates.

Galao et al. (2013) [11] studied strain and damage sensing capabilities of a carbon nanofiber cement composite and studied the effect of parameters such as curing age, loading rate, and the maximum stress applied, on strain sensing response. They reported no discernible strain sensing for samples cured at 7 days and 14 days and attributed it to the lack of proper bonding between the fiber inclusion and matrix. They also argued that a minimum current density is required for any significant strain sensing. They reported an increase in $\Delta R/R_0$ with increasing volume fraction of carbon fibers and stated that a proper dispersion of the fiber is required for efficient strain sensing .A damage sensing indicator based on the height and breadth of the peaks formed by the $\Delta R/R_0$ vs. strain relationship was suggested.

Similar studies were conducted by Wen and Chung. (2001) [6] who investigated the application of cement paste with small volume of carbon fibers as an effective strain sensing coating applied either on the tension side or on the compression side under flexural loading. The electrodes were fixed on the either side of the beam and silver paint was used to improve the contact with the specimen with DC current used with the electrodes in a four-probe configuration. They reported that the resistance in the tension side increased irreversibly for the first cycle and then, increased reversibly upon the application of flexural load with every cycle. Similarly for compression side, the resistance decreased with increasing flexural load. They also observed that the $\Delta R/R_0$ value in the tension zone was much more significant as compared to that in the compressive zone.

Azhari and Banthia (2017) [12] also investigated the effect of carbon fiber content, cement hydration and electrode type on the efficiency of carbon fiber reinforced cementitious composite as a strain sensing material and reported that above the percolation threshold, the effect of the hydration and the microstructure development on the conductivity of the composite is negligible. They also concluded that above the percolation threshold, sensing was more sensitive to tension than compression, as change in resistivity in the tension zone was guided by the fiber-to-fiber contacts. However, below the percolation threshold, the fiber matrix contact also had a significant effect on the resistance of the composite.

1.5.2 Steel Fiber Reinforced Cementitious Composites

Yoo et al. (2015) [13] investigated the flexural response of the cement composite reinforced with steel fiber under quasi-static and impact loads. They considered normal strength concrete (NS), high strength concrete (HSC) and ultra-high strength concrete (USHC) with four different volume fractions (0, 0.5, 1.0 and 2.0%) of steel fibers. They observed that the addition of fiber has an insignificant effect on the compressive strength and modulus of elasticity but a significant improvement was observed in the strain capacity at peak stress. The flexural strength increases with increasing fiber content in the order of NS, HSC and UHSC. They also observed that the flexural strength increased by 1.5 times for HSC and 3% for UHSC when compared to NS which was attributed to the crack bridging effect of fibers.

Wen and Chung (2003) [14] conducted a comparative study between steel fiber reinforced cement composite and carbon fiber reinforced cement composite. Steel fiber with average length of 6 mm and carbon fiber with average length of 15 μm was used.

They reported that resistivity increased with repeated tensile stress cycling whereas it decreased with increasing compressive stress cycling for both steel fiber and carbon fiber reinforced composites. They argued that the interface is inherently weak and is thus more sensitive to compressive force which tends to close the voids at the interface whereas tensile force would enhance the separation. This was stated as the most significant factor beside the percolation threshold where the resistivity is guided by the fiber-matrix interface. However, above percolation threshold, it was solely guided by the contact resistance between the fibers. Steel fibers are more ductile when compared to carbon fiber and thus were more sensitive to change between the fiber-fiber contacts rather the fiber-interface contact. Similar studies were conducted by [7], [10], [11], [13]–[20].

1.5.3 Novel Iron Carbonate Based Binder

Das et al. (2014) [22] reported a novel iron carbonate based binder developed by carbonating the waste metallic iron powder. The successful mixture proportion contained 60% iron powder, 20% fly ash, 8% limestone powder and 10% metakaolin by mass. Oxalic acid was added to facilitate the dissolution of iron powder and a water-to-powder ratio (w/p) of 0.24 was adopted. They observed that waste iron powder when mixed with minor components such as fly ash, metakaolin and limestone, and carbonated in a chamber for certain duration produced a sustainable novel binder with acceptable mechanical properties. They reported an average compressive strength of 30-35 MPa after 4 days of carbonation.

In another study by Das et al.2014 [23], they observed that the total pore volume decreases with increase in carbonation duration from 1 to 4 days while the critical pore sizes remained relatively constant. Also, the fraction of larger pores and the average pore

size significantly decreased with increasing carbonation duration. But when compared with 28 days cured OPC pastes, the total pore volume was lower in iron carbonate based binder but the critical pore sizes were larger. Secondary and back scattered imaging revealed reaction products on the surface of iron particle and on the surface of fly ash. The reaction product was determined to be comprised of complex carbonate consisting of iron, carbon, silicon, aluminum and calcium.

To study the effect of high temperature on the iron carbonate based novel binder, Das et al (2016) [24] quantified the thermal decomposition of the material. They reported that the iron carbonate complex decomposed at 300^{o} C while the calcite mostly decomposed at around 600^{o} C. At higher temperature, they also observed formation of stable phases of hematite and magnetite. There was an increase in porosity when the temperature was increased to 300^{o} C due to the decomposition of the major carbonate and there was a slight reduction in porosities when the temperature was increased further. Higher temperature led to the refinement of pore structure as the critical pore sizes reduced by a factor of 7 and the fraction of finer pores increased by a factor of 10.

Chapter 2: Experimental Program

2.1 General Background

The capability and efficiency of cementitious composite reinforced with metallic particulate as a strain sensing material has been studied. The mixture proportions and the development of experiment setup are explained in this chapter.

2.2 Experimental Program:

2.2.1 Materials, Mixing and Casting of Specimens

For plain cement mortar**,** commercially available Type I/II ordinary Portland cement (OPC) conforming to ASTM C 150 was used. The chemical composition of the cement is presented in Table 1.

Table 1: Chemical Composition of OPC

Composition	SiO_2	Al_2O_3	Fe_2O_3	CaO	MgO	SO_3	Na_2O	K_2O	LOI
Amount (%)	21	3.61	3.47	63	3.26	3.04	0.16	0.36	2.13

For the mortar mixture, natural silica sand with an average particle size of 0.6 mm was used. Plain cement mortar was casted in form of polypropylene beam molds (127 mm (length) x 25.4 mm (depth) x 25.4 mm (width)) and was cured for 28 days in the curing room with >98% RH. The water-to-cement ratio (w/c) was maintained as 0.40 by mass. Figure 1 presents the particle size distributions of metallic iron powder and Ordinary Portland Cement (OPC). Prior to preparation of mortar mixture, the desired proportion of the raw solid materials (OPC, sand and iron powder) were measured and hand mixed for two minutes. Water was then added in small batches while simultaneously mixing in a

mechanized mixer. The mixture was then poured into the molds and vibrated by placing on a table vibrator until the desired compaction was achieved.

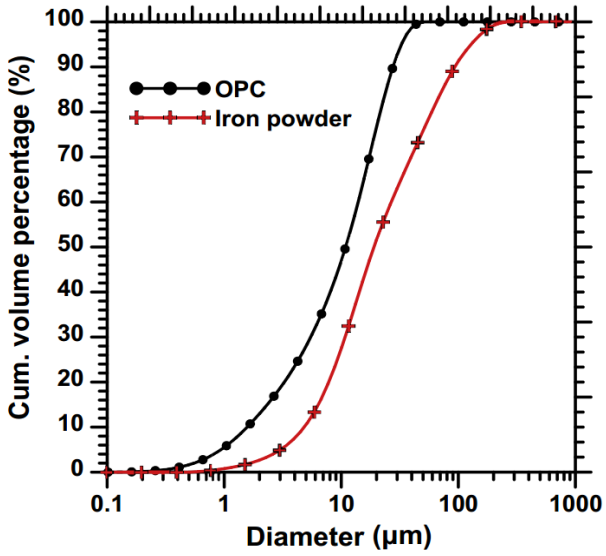

Figure 1: Particle size distributions (PSD) of ordinary portland cement and metallic iron powder

For metallic particle reinforced cementitious systems, four different replacement volumes (10%, 20%, 30% and 40% by volume of cement) of iron powder were considered and cast as described earlier. Metallic iron powder with a median particle size of 19.03 μm (as shown in Figure 1) is utilized as starting material which is a waste generated during the structural steel is shot blasting. The iron powder contains 88% Fe and 10% oxygen (due to atmospheric oxidation) along with trace amounts of Cu, Mn and Ca as determined from particle induced X-ray emission spectroscopy (PIXE). The iron powder is elongated and angular in shape (Figure 2) which enhances the reactivity owing to the large surface area to volume ratio of the powder. The elongated shape also facilitates fiber like behavior, thereby potentially helping strain sensing.

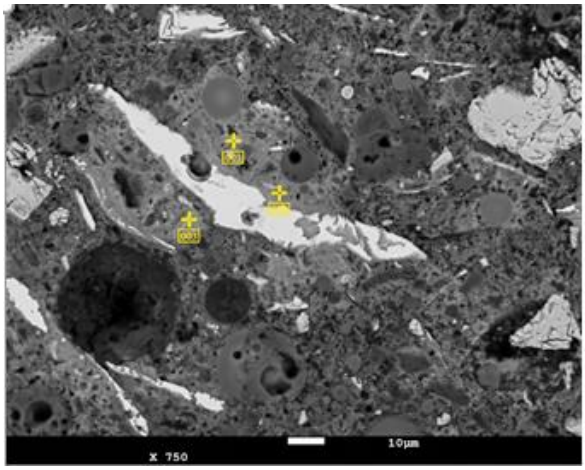

Figure 2: Scanning electron micrograph of iron particles (bright white particles) with the scale bar corresponding to 10 µm

Class F fly ash and metakaolin conforming to ASTM C 618 and limestone powder (with median size of 0.7µm) conforming to ASTM C 568 was also used along with iron powder for the synthesis of the binder. Fly ash was used a source of silica for the reactions (to potentially facilitate iron silicate complexation [25] whereas limestone provides nucleation sites for the product to form. Metakaolin was used as a rheology modifier [22]. In this process of iron carbonation, water is only a mediator in the reaction, acting as a medium of mass transfer and does not participate in the reaction chemically. Further minimization of water demand without compromising the consistency and cohesiveness of the mix was achieved using metakaolin. To prevent oxidation and enhance iron dissolution, oxalic acid (a weak acid) is used as an organic reducing agent/chelating agent for metal cations. Chemical compositions of fly ash and metakaolin determined using X-ray fluorescence (XRF) spectroscopy are presented in Table 2.

Table 2: Chemical composition of fly ash and metakaolin used in iron carbonate matrix

Component (%)	Fly Ash	Metakaolin
SiO_2	59.52	39.42
Al_2O_3	23.03	8.5
Fe_2O_3	4.62	0.37
CaO	4.87	35.53
MgO	-	12.63
SO_3	0.48	2.89
Na_2O	2.32	1.7
K_2O	-	0.39
LOI	0.37	-

Figure 3 presents the particle size distributions of iron powder, fly ash, metakaolin and limestone which were determined using dynamic light scattering. All the ingredients are finer than the iron powder used.

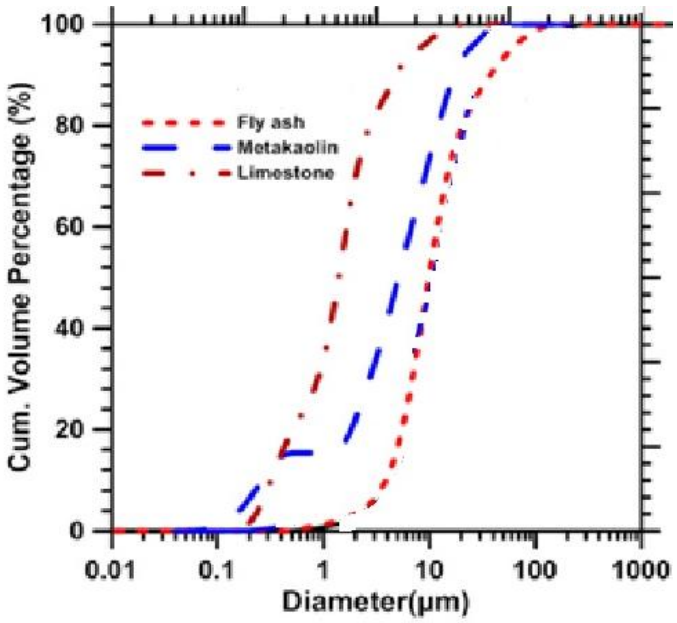

Figure 3: Particle Size Distribution (PSD) of fly ash, metakaolin and limestone

The mixture proportion used for the iron carbonate based novel binder is 64% iron, 20% fly ash, 8% limestone and 6% metakaolin with water-to-solid ratio (w/s) of 0.24 by mass which was decided in accordance with earlier studies.

Prior to preparation of iron carbonate mixture, the desired proportion of the raw solid materials (iron powder, fly ash, metakaolin, limestone and oxalic acid) was dry mixed for two minutes until a homogenous mixture was obtained. The water was mixed with measured oxalic acid and introduced into the mixer. The mixture was then poured into the mold and vibrated by placing on a table vibrator until the desired proper compaction was achieved. Since the carbonation process of iron does not utilize water for the formation of reaction product, the water content was solely based on obtaining the desired workability.

Prismatic specimens with dimensions of 127 mm (length) x 25.4 mm (depth) x 25.4 mm (width) were prepared in polypropylene molds and immediately placed inside the carbonation tank with 100% CO_2 in room temperature inside a fume hood. The carbonation tank was developed specifically for the project as shown in Figure 4. A generic 27-gallon storage tank with a sealing lid and extra thick walls was selected. The tank was lined with a window sealant to improve the seal between the lid and the sides so as to maintain CO_2 saturation in the tank. Industrial clamps were used to further improve the sealing. The lid was reinforced with wooden planks so that the lid does not balk due to pressure of CO_2 gas. The tank was purged with CO_2 every 4 hours. The tank was also fitted with safety valve, a gas inlet cap and a gas outlet cap for letting in the CO_2 gas in and the air out.

Figure 4: Carbonation tank developed for iron carbonate binder synthesis

The samples were demolded after one day of carbonation in order to attain enough strength so as to strip the mold without causing damage to the specimen. After demolding, the beams were again placed in a 100% CO_2 environment in the tank for 21 days. The tank was saturated with 100% CO_2 every 4 hours after expunging the air. Also, once in two days, the tank was opened and the water, which is collected at the bottom, removed. After the respective duration of CO_2 exposure, the samples were placed in air at a room temperature to allow the moisture to evaporate for 6 days.

The plain cement mortar, metallic reinforced cement mortar and novel iron carbonate based binder, after their respective curing durations, were saturated by keeping it

submerged in water for 24 hours to obtain a completely saturated system for electrical property testing.

2.2.2 Test Methods

Flexural Strength Testing

The flexural strength test was carried out on the particulate reinforced cement composite and iron carbonate samples. After the curing regimen of 28 days for cementitious composites and 14 days in 100% CO_2 environment with the air exposure time of 7 days for iron carbonate samples, prismatic specimens were cut in half to obtain beams 63.5 mm (length) x 25.4 mm (depth) x 25.4 mm (width). These beams were fully saturated by keeping them submerged in water for 24 hours. The three point bending test was conducted as shown in Figure 5 and the load and displacement were recorded using NI LabVIEW data acquisition software. A displacement rate of 0.380 mm/min was maintained for all the flexural tests. The load head and the supports were taped with thin elastic film to insulate them before the electrical impedance testing.

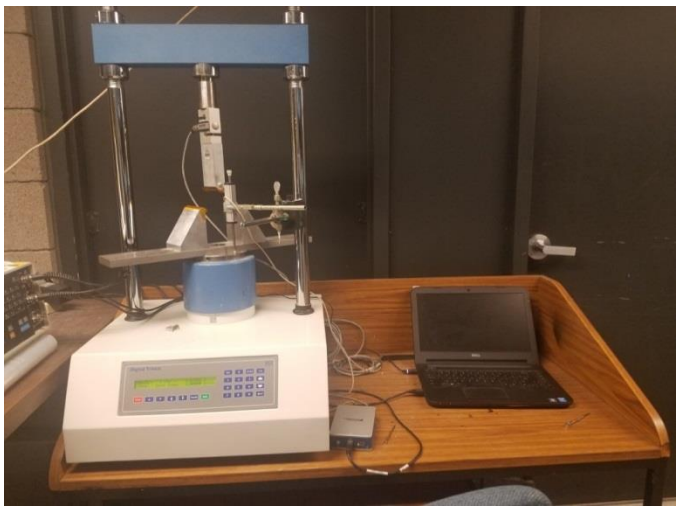

Figure 5: Three point bending ELE frame setup for flexural testing

Electrical Impedance Spectroscopy

The electrical response of the specimens before and after loading was determined using electrical impedance spectroscopy (EIS). The EIS spectra were obtained using a SOLARTRON 1260 gain phase analyzer (as shown in Figure 6) operating at a frequency range of 1 Hz to 10^7 Hz. A 250 mV AC signal was used. The meeting point of bulk and electrode arcs in a Nyquist plot (plot of real vs imaginary impedance) is denoted as the bulk resistance (R_b). The effective conductivity of the specimen (σ_{eff}) was calculated as:

$$\sigma_{eff} = \frac{L}{R_b A} \quad (1)$$

Where, L is the length and A is the cross sectional area of the specimen. EIS was carried out using small input signals so as to ensure that the response is pseudo-linear (i.e., the current response to a sinusoidal voltage response is sinusoidal with a shift in phase).

Figure 6: SOLATRON ™ 1260 gain phase analyzer

Electrical Impedance Setup

The electrical connection consists of 2 copper plates of size 25.4 mm x 25.4 mm as shown in Figure 7, and was attached at the end of the sample. The copper plates were soldered together with the open end of an alligator clip to create the electrode. The length of the wire was minimized to prevent lead wire impedance effects.

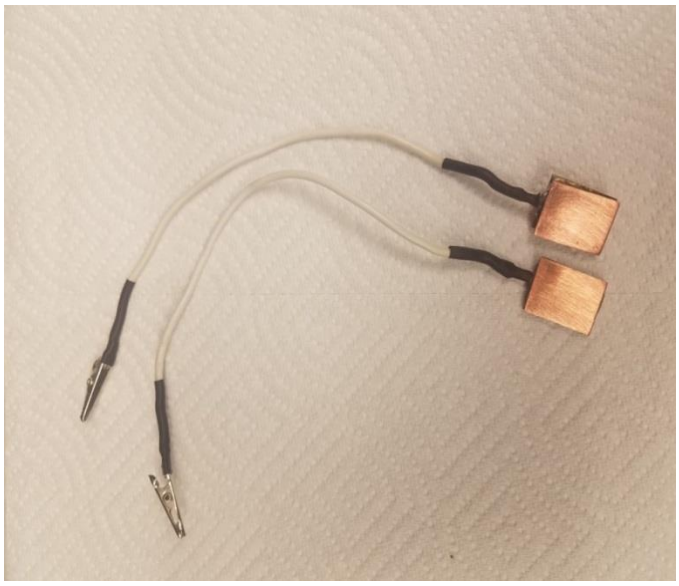

Figure 7: Copper electrodes for electrical measurements

Before placing the electrode, a conducting medium was introduced between the samples to improve the conductivity of the contacts. Silver paint was adopted first as the conducting medium. However, the Nyquist data obtained indicated a lower signal-to-noise ratio. Wet cleaning sponge was also considered but no improvement was obtained. Wet paper towel between the electrodes and the samples was found to be more effective as a conducting medium and thus used for all the tests.

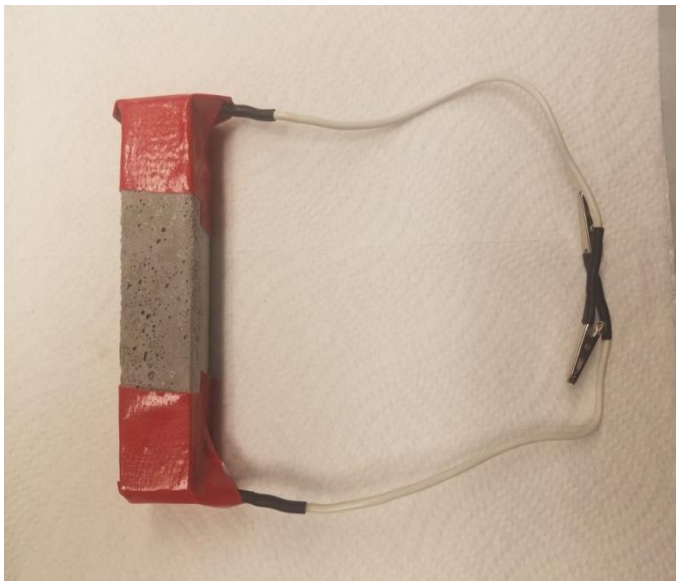

Figure 8: Prepared sample with electrode attached

Figure 8 presents the final prepared sample setup adopted for the strain sensing. The paper towel was kept between the electrodes and the specimen ends were sealed using insulating tape. Care was taken so that the wet paper towel does not drip water. The electrode was scrapped with sand paper after each experiment to remove the layer of oxide and to avoid any contamination.

Strain Sensing

The specimen with electrodes was carefully placed in the loading frame. Care was taken so that no sharp edges on the sample damage the insulating tape on the support. The complete experimental setup is presented in Figure 9.

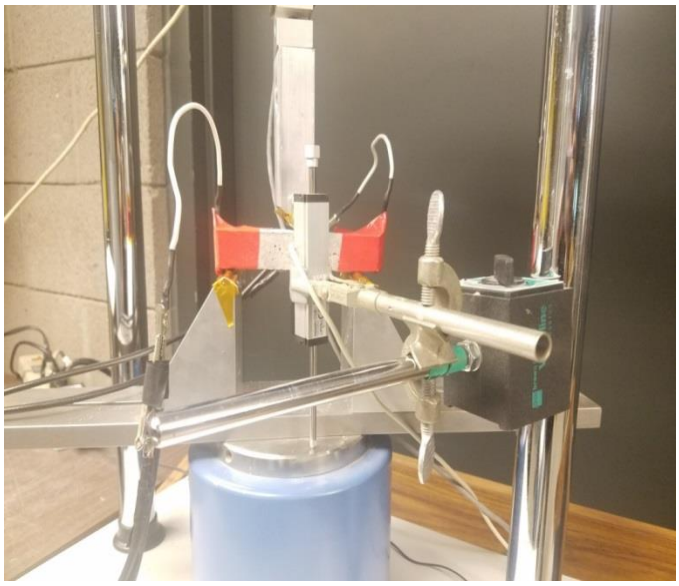

Figure 9: The complete experimental setup of strain sensing procedure

The sample was mounted on the support and the impedance analyzer was used to obtain the impedance of the sample in an unloaded state. Four different loads were used, and impedance measured while the specified load was maintained on the sample.

Under a certain load, a potential sweep was carried out using the impedance analyzer and the impedance data was recorded. The loading profile is provided in Figure 10.

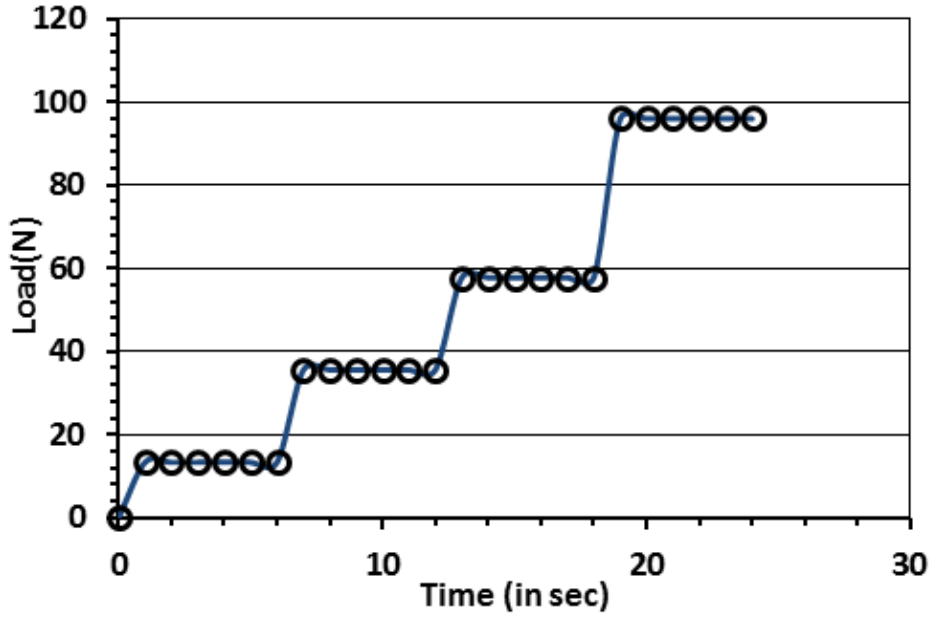

Figure 10: The representative loading profile for strain sensing measurements

2.3 Nyquist Plot

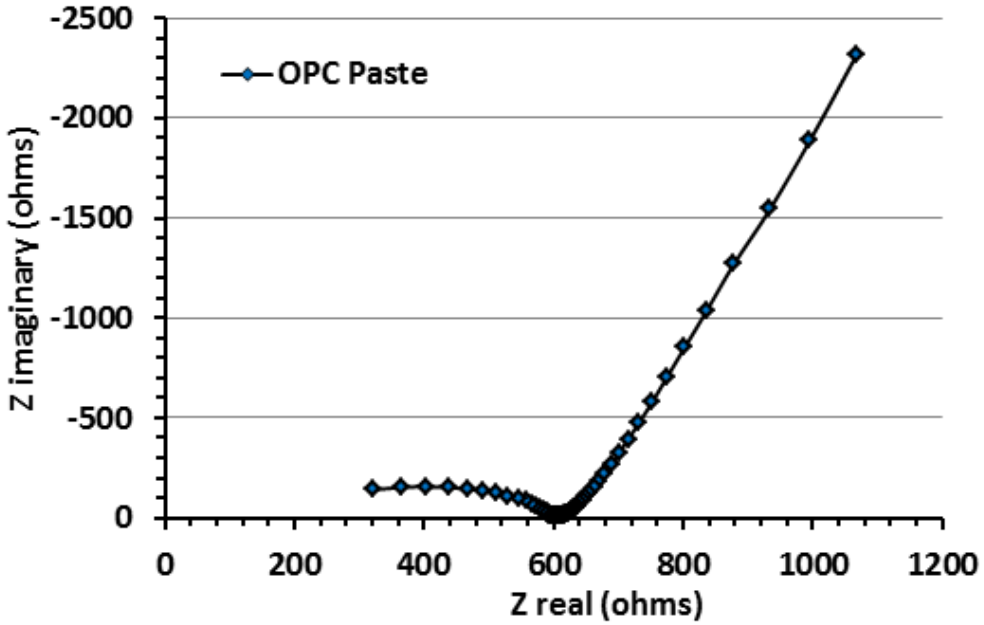

Figure 11: Typical Nyquist plot for a plain cement paste

A typical impedance response of a cement paste is shown in Figure 11 where the imaginary part of impedance is plotted against the real part (Z). This is known as a Nyquist plot. The frequencies increase from right to left where low frequencies represent the electrode properties and high frequencies represent the bulk material response. The shape of the Nyquist curve could help in discerning the possible mechanisms of electrical conduction. Theoretically, a single semi-circle in Nyquist plot is characteristic of a single "time constant" but due to microstructural artifacts only a portion of one or more semicircles is observed. To extract the electrical properties from the Nyquist response, it is generally fitted with an equivalent circuit model[26]. For the plain mortar, a typical electrical circuit model which is extensively used in literature was used. For the metallic reinforced cement mortar and for the iron carbonate binder, a modified equivalent electrical circuit model was developed which was found to fit the experimental data well. The equivalent circuit models are provided in the following chapter.

Chapter 3: Strain Sensing Responses of Matrices Containing Metallic Inclusions

This chapter discusses the experimental results on strain sensing studies carried out on metallic particulate reinforced cement composites as well as iron carbonates. The resistances of the matrices with and without imposition of load, the fractional change in resistances, and the microstructural model to extract a characteristic resistance are described.

3.1 Mechanical Strength

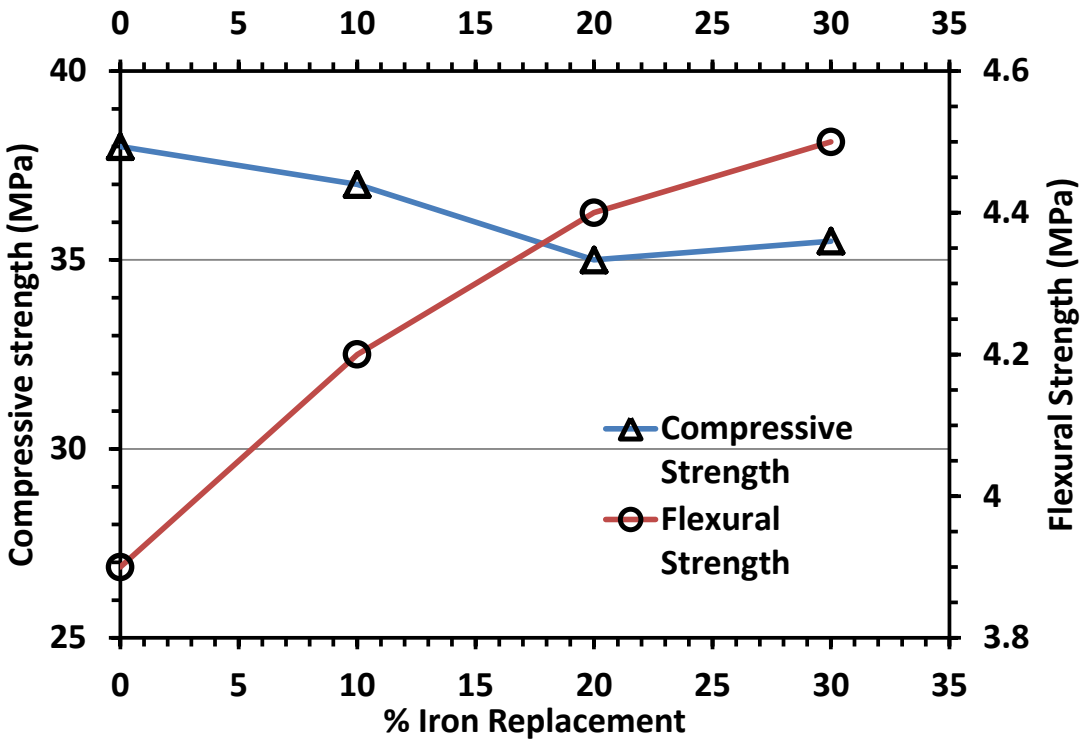

Figure 12: Compressive and flexural strength for 0%, 10%, 20% and 30% of iron powder replacing cement in mortars

Figure 12 shows the compressive and flexural strengths of mortars for all four iron powder replacement (of cement) levels. It is observed from Figure 12 that the compressive strength remains relatively unchanged with an increase in iron powder

replacement level from 0% to 40% [27]. However, significant improvement was observed in case of flexural strength, which was due to the presence of elongated iron fiber acting as a micro-reinforcement in the microstructure. The compressive strength decreased by 6% between plain cement mortar and 30% iron powder replacement whereas flexural strength increased by 18% between the plain cement mortar and 30 % replacement of iron powder. Thus, iron powder reinforced cement composites can be used as construction materials without adversely affecting the mechanical properties. For the iron carbonate based binder, the flexural strength was around 8 MPa and the compressive strength, around 28 MPa.

3.2 Nyquist Plot for Matrices Containing Metallic Inclusion

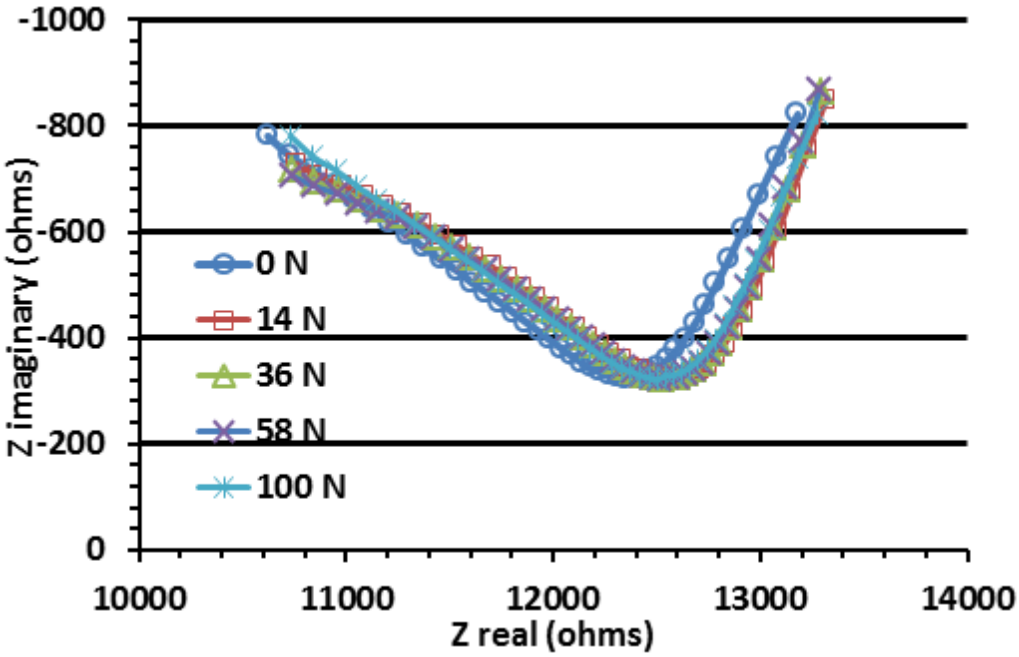

Figure 13: Nyquist plot of OPC mortar as a function of applied load

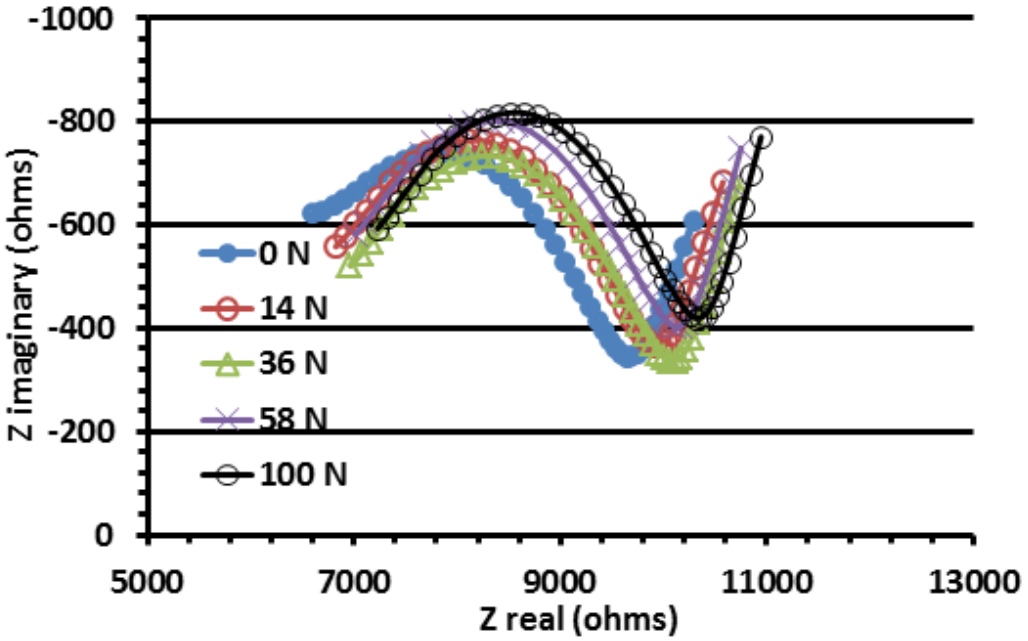

Figure 14: Nyquist plot of mortar with 40% iron powder replacement as a function of applied load

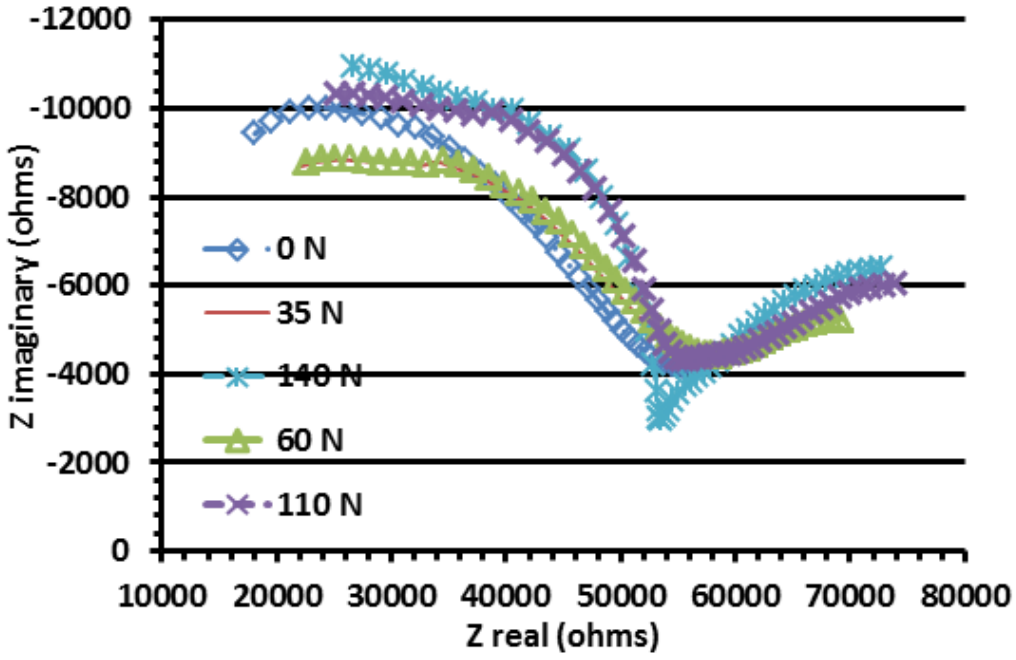

Figure 15: Nyquist plot of iron carbonate as a function of applied loads

Figure 13 shows the Nyquist plot for the OPC mortar as a function of applied loads, while Figures 14 and 15 show the Nyquist plots for mortars with 40% cement replacement with iron powder, and the iron carbonate based binder respectively, as a function of different loads. As is evident from Figures 13-15, the Nyquist plot generally shifts towards the left as the applied load is increased, representing a decrease in resistivity. It is clear that the plain cement mortar has no significant strain sensing capability as the Nyquist plots are rather invariant with load. For the case of mortar with 40% iron powder replacement, the leftward shift is more prominent. Thus, it is evident that conducting particulates change the electrical response of the system under load, and thus provides the potential for strain sensing. To extract the physical parameters of the microstructure relevant for electrical property modeling, circuit models were developed, as explained in the forthcoming section.

3.3 Equivalent circuit development

Electric circuit development is an efficient method to model the impedance results in terms of Resistors (R), Capacitors (C) and inductors (L).In equivalent circuit methodology, resistance is commonly used to describe the conductive or (resistive) pathways for ionic and ohmic conduction. Capacitors are used to represent the processes of polarization such as double layer polarization. The overall electrical characteristics can be described as: resistive part due to the resistance of the constituents and the bulk in the mortar, and the capacitance due to the electrical interfaces, especially between the pore network and adjoining solids in concrete. The bulk part therefore can also be represented using simple equivalent electrical circuits [26], [28].

For the purpose of developing the electrical circuit, the microstructure in a plain cement paste system is considered to have three electrical paths [29], [30]:

- Continuous conductive path (CP) which consists of a sustained connection of micro-pores. It consists mainly of connected capillary pores, either through pore necks or direct connection. Here, the current conduction mechanism is ionic, due to the presence of ions such as $Ca^{2+,}$ Mg^{2+}, Na^{2+}, and OH^{-} and thus can be represented by ohmic law.
- The discontinuous micro-pores (DP) consist of pore networks which are intercepted or hindered by the presence of hydration products or unreacted cement particles. The discontinuous pores also hamper the connectivity of the connected pores.
- A purely insulating path consisting of unreacted cement particles and other non-conducting particles depicted as (IP).

Figure 16 and 17 represents all the possible paths which the electric current can take while traversing any cement based material.

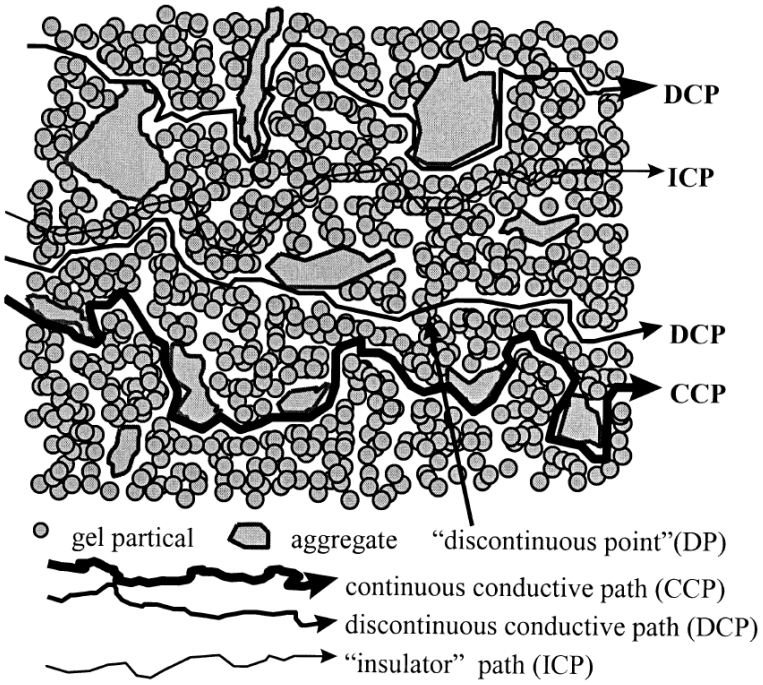

Figure 16: Schematic representation of the paths in electrical conduction in cement based materials [29], [30]

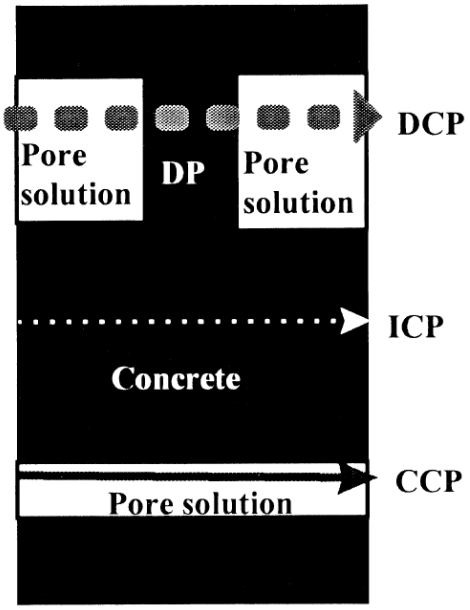

Figure 17: A simplified microstructural representation of electrical conduction in concrete [26]

Figure 18 shows the equivalent electric circuit model used for a plain OPC system based on the discussion above. The bulk resistance of the sample corresponds to the resistance of the connected pores. In the Figure 18, R_1 is the electrode resistance, R_2 is the resistance of connected pore, R_3 is the resistance offered by the wet paper towel between electrode and sample, R_4 is the resistance attributed to unconnected or isolated pores, C_1 is the capacitance related to the interface of solid phases and C_2 is the capacitance associated with the interface between pore wall and bulk pore solution.

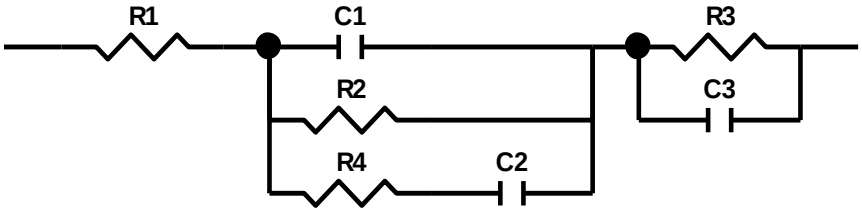

Figure 18: Electric circuit models for cement mortar

For matrices containing iron powder, which is a conductive material, an additional parallel conduction path is added to the circuit to represent the conducting particles. The bulk resistance is taken as the equivalent resistance of the connected pore and iron particles in parallel. Figure 19 shows the equivalent circuit model used for the metallic powder reinforced mortar.

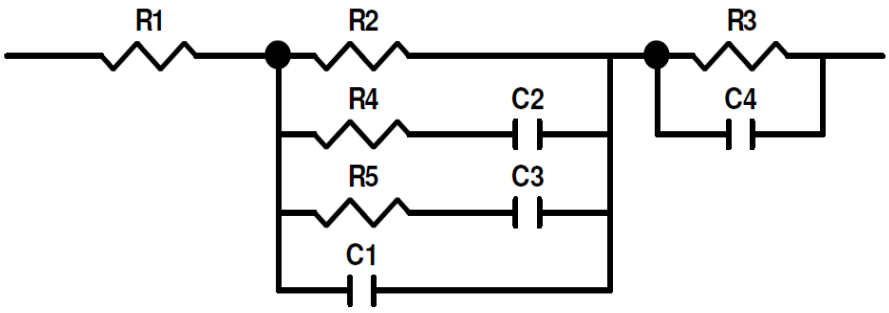

Figure 19: Electrical circuit models used for particulate reinforced cement composite

In the Figure 19, R_1 is the electrode resistance, R_2 represents the resistance of connected pore, R_3 is resistance offered by the wet paper towel between electrode and sample, R_4 is the resistance attributed to the unconnected or isolated pores, R_5 is the resistance of iron powder, C_1 is related to the interface of solid phases, C_2 is the capacitance associated with the interface between pore wall and bulk pore solution, C_3 is due to the interface between iron powder and bulk solid and C_4 is the capacitance of the interface between electrode and sample.

The circuit model parameters were extracted using ZView software with circuit fitting capabilities. Typical values of the parameter extracted for plain cement mortar, cement mortar with 40% iron powder replacing cement, and iron carbonate before the application of load are tabulated in Tables 3 and 4.

Table 3: Values for the circuit model parameters for cement mortar

R_1	R_2	R_3	R_4	C_1	C_2	C_3
4 Ω	11885 Ω	300 Ω	110050 Ω	1.12×10^{-11} F	1.36×10^{-10} F	3.10×10^{-12} F

Table 4: Values for the circuit model parameters for cement mortar with 40% iron powder replacing cement and iron carbonate binder

Composite	R_1	R_2	R_3	R_4	R_5	C_1	C_2	C_3	C_4
40% iron powder composite	4 Ω	8960 Ω	300 Ω	38611 Ω	56240 Ω	1.36 x 10^{-11} F	1.56 x 10^{-10} F	1.15 x 10^{-9} F	3.10 x 10^{-12} F
Iron carbonate	4 Ω	47810 Ω	300 Ω	149190 Ω	55430 Ω	2.56 x 10^{-12} F	3.35x 10^{-11} F	6.49 x 10^{-12} F	3.10 x 10^{-12} F

3.4 Effect of Applied Load (Stress) on the Electrical Properties of Metallic Reinforced Cementitious Composites

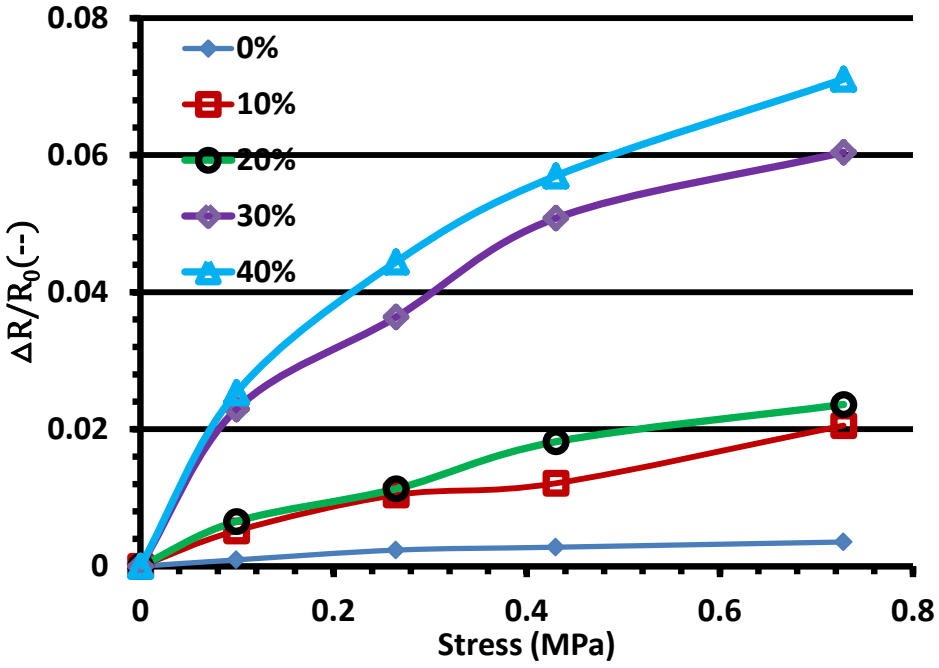

Figure 20: $\Delta R/R_0$ vs stress (MPa) for cement mortar with 0%, 10%, 20%, 30% and 40% iron powder as replacement for cement

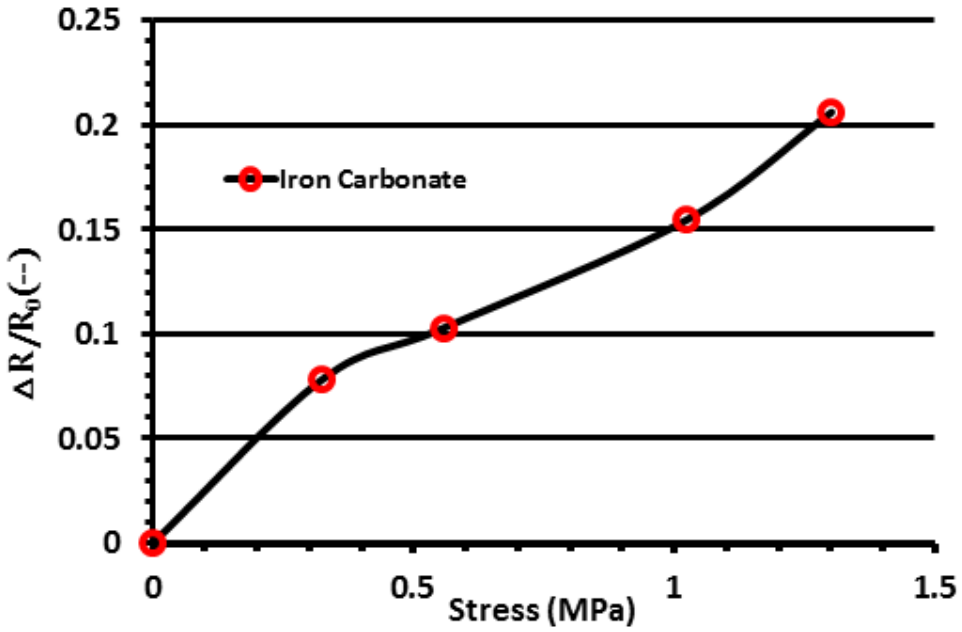

Figure 21: $\Delta R/R_0$ vs stress (MPa) for iron carbonate

Figure 20 shows the fractional change in resistance ($\Delta R/R_0$) as a function of applied stress for mortars with different amounts of iron powder replacing cement. It can be observed from Figure 20 that the fractional change in resistance increases with increasing iron powder dosage, attesting to the efficiency of the metallic reinforced cementitious composite in sensing strain. Similar observations were reported in studies conducted by Azhari and Banthia (2017) [12]. As the iron powder percentage is increased, the resistance is primarily guided by the continuous connected paths created either by particulate contacts or by the contacts between particulates and the pore solution. For fiber reinforced composites, studies have shown that the fiber-fiber contact is more sensitive to flexural response when compared to the fiber–interface contacts (which is more sensitive to compression loading) and thus, the efficiency of the metallic cementitious composites to acts as a strain sensor increases with increase in the

percentage of the conductive component [7], [12], [17]. However, it should be noted that the metallic particulate composite with a low replacement level of cement by iron powder (10% or 20%) also depicts significant sensitivity to strain (or applied load) and thus, it is not necessary to reach the percolation threshold to obtain a strain sensing cementitious composite. Figure 20 also reinforces the hypothesis that the presence of a conductive component amplifies the strain sensing capability of a plain cement mortar [7] as for an applied stress of 0.43 MPa, $\Delta R/R_0$ increases by 335 % between plain cement mortar and mortar with iron powder replacing 10% of cement.

Similar trend was also observed for iron carbonate based binder where resistance increases with applied stress (Figure 21). The iron carbonate binder has unreacted iron particles as reported by Das et al. (2014) [31] which act as conducting media and renders strain sensing capability to the iron carbonate based binder. Figure 23 shows the fractional change in resistance, $\Delta R/R_0$ for the iron carbonate matrix with increasing applied stress. It is noticed that this value, which is an indication of strain sensing capability, is higher for the iron carbonate than for the particulate reinforced composites, primarily because of the higher amount of conductive iron particles in the iron carbonate binder.

3.5 Gage Factor

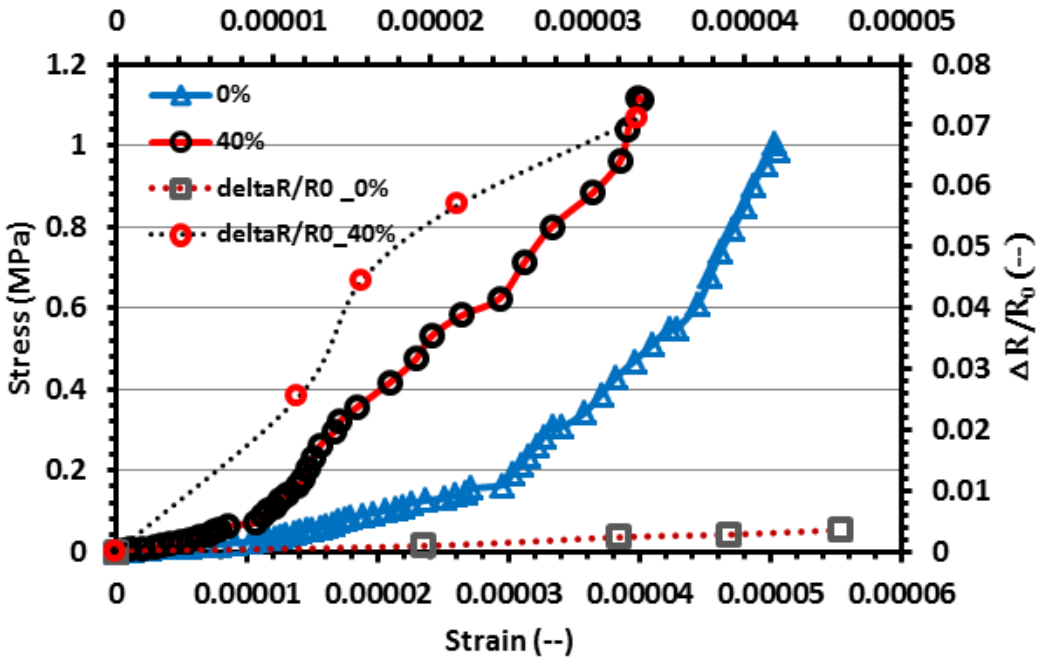

Figure 22: Stress-strain-$\Delta R/R_0$ for plain cement mortar and cement mortar with 40% iron powder replacement for cement.

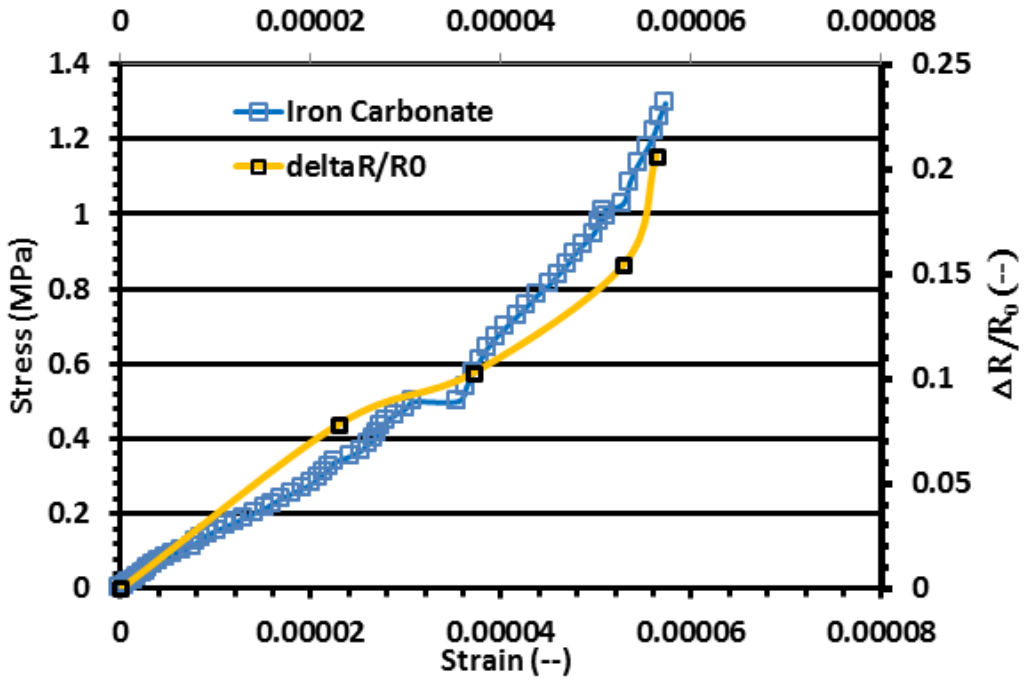

Figure 23: Stress-strain-$\Delta R/R_0$ for iron carbonate based binder

Figures 22 and 23 represents the relationship between applied stress, strain, and the fractional change in resistance for the plain cement mortar, cement mortar with 40% iron powder replacing cement, and the iron carbonate based binder. One of the prominent methods to quantify the sensitivity or efficiency of strain sensing is by calculating the gage factor. Gage factor is the defined as the ratio of fractional change in resistance to the strain [12], and is given as:

$$GF = \frac{\frac{\Delta R}{R0}}{\in} \quad (2)$$

The higher the gage factor, higher is the strain sensing efficiency and thus, it can be a useful indicator of the applicability of the sensor [12], [32]. Table 5 presents the range of values for the gage factor for the composites evaluated in this study. It is evident from Table 5 that the efficiency of strain sensing increases with increasing iron replacement percentage. Also, it is noted that the iron carbonate based binder is more efficient when compared to iron powder reinforced cementitious composites. For comparison, Chung (2002) [21] reported gage factors of approximately 4560 (tension side) and 200 (compression side) for 0.72% volume fraction steel fiber in cement paste, and approximately 1290 (tension) and 720 (compression) for 0.3% volume fraction of steel fiber in cement paste. Banthia and Azhari (2017) [12] reported gage factor of 1250 (in tension) for carbon fiber reinforced cementitious composites containing a 15% volume fraction of fibers with an average length of carbon fiber 0.24 inches. As observed, the gage factors vary with the type of fibers used and the loading procedure. However, carbon fibers and steel fibers are expensive products which would increase the overall cost of production of the composite whereas iron powder is waste product and is shown

in the presented results to have similar or better efficiency in strain sensing when used in cementitious materials.

Table 5: Gage factor for metallic cementitious composite and iron carbonate based binder

Composite	Gage factor Range
Plain cement mortar	47-76
10% Iron replacement cementitious composite	393-477
20% Iron replacement cementitious composite	511-631
30% Iron replacement cementitious composite	1690-2250
40% Iron replacement cementitious composite	2140-2850
Iron Carbonate based binder	2776-3424

Chapter 4: Extracting Fundamental Electrical Properties for Use in FE Modeling

This chapter discusses the methodology to extract the electrical properties to be used in the finite element (FE) modeling of strain sensing response of particulate reinforced cementitious composites. The model formulation and simulations are part of the next chapter.

4.1 Effective Media Theories and Drawbacks

Conventionally, effective electrical properties of composites are calculated using effective media theories (EMT). EMT or any other mean field theory is a physical model based on the individual properties of the components and their respective volume fractions in the composites [33]–[36] . Usually electrical conductivity and permittivity are calculated using the EMT. Some of the most frequently used EMT are [37] :

- Maxwell model

$$\varepsilon_{eff} = \varepsilon_h + 3f \frac{\varepsilon_i - \varepsilon_h}{\varepsilon_i + 2\varepsilon\_h} \varepsilon_h \quad (3)$$

- Maxwell-Garnet model

$$\varepsilon_{eff} = \varepsilon_h \frac{1 + 2f\left(\frac{\varepsilon_i - \varepsilon_h}{\varepsilon_i + 2\varepsilon_h}\right)}{1 - f\left(\frac{\varepsilon_i - \varepsilon_h}{\varepsilon_i + 2\varepsilon_h}\right)} \quad (4)$$

- Symmetric Bruggeman model

$$\varepsilon_{eff} = \frac{1}{4}[3f(\varepsilon_i - \varepsilon_h) + 2\varepsilon_h - \varepsilon_i + ((1 - 3f)^2\varepsilon_i^2 + 2(2 + 9f - 9f^2)\varepsilon_i\varepsilon_h + (3f - 2)^2\varepsilon_h^2) \quad (5)$$

- Asymmetric Bruggeman model

$$\frac{\varepsilon_i - \varepsilon_{eff}}{\varepsilon_i - \varepsilon_h} = (1 - f)\left(\frac{\varepsilon_{eff}}{\varepsilon_h}\right)^{\frac{1}{A}} \quad (6)$$

- Looyenga model

$$\varepsilon_{eff} = \left[\left[(\varepsilon_i^{\frac{1}{A}} - \varepsilon_h^{\frac{1}{A}})f + \varepsilon_h^{\frac{1}{A}}\right]\right]^A \quad (7)$$

In the above models,

ε_{eff} = effective dielectric constant of medium

f = volume fraction of the filler

ε_i = dielectric constant of filler

ε_h = dielectric constant of host

A = depolarization factor or a constant depending on shape of inclusions (2 for disk fillers and 3 spherical fillers).

Cementitious systems often have complex distribution of phases and thus, calculating effective properties using EMT is cumbersome and erroneous in many instances. Also, they are accurate only for low volume fractions of inclusions and result in erroneous predictions at or near the percolation threshold in multi-phase materials [38]. Percolation theory is used to offset this disadvantage of EMT. It is used to describe the response of disordered systems with higher volume fractions of inclusions in. Percolation theory has little or no statistical dependency and explicitly takes into the account the distribution, shape, size and orientation of the minor phase. Percolation theory is defined using percolation threshold. Percolation threshold is that critical volume fraction of the inclusions where significant changes occurs in the physical and electrical properties of

the composite [33][36]. At percolation threshold, a simple power law can be used to capture the changes in the properties of the composite:

$$\frac{\varepsilon}{\varepsilon_h} = (f - f_c)^{-s} \quad (8)$$

where, ε is the dielectric constant of composite, ε_h is the dielectric constant of the host matrix, f_c is the percolation threshold and f is the inclusion volume fraction. The percolation threshold is not easy to calculate especially in complex systems, which seriously limit its applicability. [39].

4.2 Extraction of fundamental electrical properties for modeling effort

The following sections elucidate the procedure to extract the fundamental electrical properties (frequency dependent conductivity and permittivity) of the phases and the interface for modelling efforts. This section gives a brief introduction to the theory of dielectric materials. The analytical equations to calculate electrical properties from Nyquist plot are also provided in the following sections.

4.2.1 Theory of Dielectric Material

The time-harmonic Maxwell's equations presented in equation (9)-(12) are the four most significant partial differential equations in the field of dielectrics [39]. The most basic premise is that the application of electrical field causes disruptions and movements in the bound and the free charges in the system. The movement in the bound charges causes polarization, which is defined by the electrical permittivity whereas the free movement of ions and electrons defines the electrical conductivity.

- Ampere's law

$$\nabla \text{ x } \vec{E} = -j\mu\omega\vec{H} \quad (9)$$

- Faraday's law

$$\nabla \text{ x } \vec{H} = j\varepsilon\omega\vec{E} + \vec{J} \quad (10)$$

- Gauss law for electric field

$$\nabla . \vec{D} = \rho \quad (11)$$

- Gauss law for magnetic field

$$\nabla . \vec{B} = 0 \quad (12)$$

where, E is the applied electric field, ω is angular frequency =2πf , f is applied frequency, H is the magnetizing field, ε is the permittivity of the sample, J is the current density, D is the electric displacement, B is the magnetic field, ρ is the charge density and → variables refers to vector field.

Equations (9) and (10) give a relationship between electric and magnetic fields in a system which can be solved by using discrete boundary equations. Equations (11) and (12) represent the Gauss law for electric and magnetic fields, which utilize flux entities described by $\vec{B}$ and $\vec{D}$ and are related as:

$$\vec{D} = \varepsilon\vec{E} \quad (13)$$

$$\vec{B} = \mu\vec{H} \quad (14)$$

where, ε represents the electrical permittivity and μ is magnetic permeability, which are material properties. These two material properties are often expressed by the relative quantities ε_r and μ_r as:

$$\varepsilon = \varepsilon_r \varepsilon_0 \tag{15}$$

$$\mu = \mu_r \mu_0 \tag{16}$$

where, ε_0 and μ_0 represent the permittivity and permeability of vacuum.

The dielectric permittivity is an important material property which measures how well the medium can be polarized in presence of an electric field. Figure 24 represents two parallel plates with a dielectric medium in between such that when an electric potential is applied between the two plates, it induces a small dipole moment in the direction opposite to the applied electric field due to separation and accumulation of charges on the plate surface. This degree of separation of charges characterizes the dielectric properties.

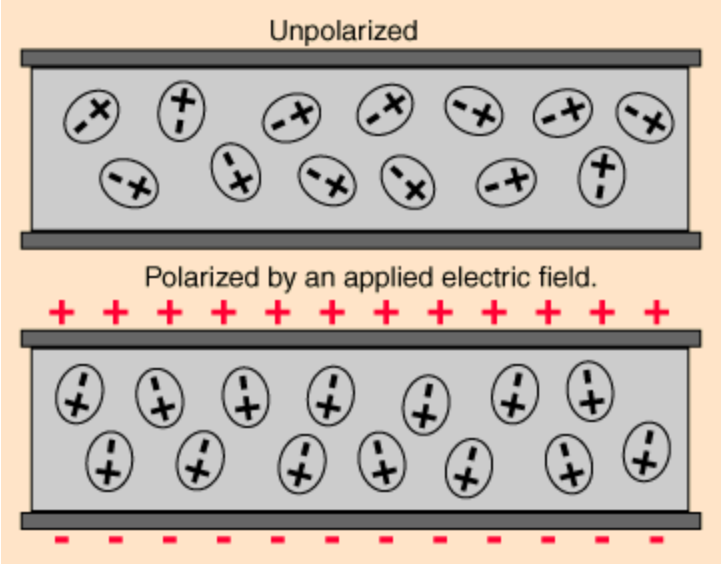

Figure 24: Representative parallel plate capacitors

For a dielectic material, the constitutive relation is given as:

$$\vec{D} = \varepsilon_\alpha \vec{E} + \vec{P} \tag{17}$$

where, ε_α=8.854x10^{-12} F/m and polarization of material P is defined as the induced dipole moment per unit volume and is assumed to be proportional to electric field as:

$$\vec{P} = \varepsilon_\alpha \chi \vec{E} \quad (18)$$

where, χ is the dimensionless dielectric susceptibility. Thus, Equation 17 can be rewritten as:

$$\vec{D} = \varepsilon_\alpha (1 + \chi)\vec{E} = \varepsilon_\alpha \varepsilon \vec{E} \quad (19)$$

The total current density, J results from an applied alternating electric field whose time dependency can be represented as $\vec{E} = \overrightarrow{E_0} \exp(i\omega\tau)$ where $\omega = 2\pi f$.

$$J = J_C + J_D \quad (20)$$

where, J_C is conduction current density and J_D is displacement current density.

And, $J_C = \sigma\vec{E}$ as defined by ohm's law and $J_D = \frac{\partial \vec{D}}{\partial t} = i\omega\varepsilon_\alpha\varepsilon\vec{E}$ as described by Maxwell equations.

Total current density can be expressed as a complex conductivity value as shown in Equation (21):

$$\vec{J} = \sigma\vec{E} + i\omega\varepsilon\varepsilon_\alpha\overrightarrow{E} = \sigma^*\vec{E} \quad (21)$$

where σ^* is the effective electric conductivity, including the effects of polarization.

In terms of complex dielectric constant, Equation 19 can be stated as:-

$$\vec{D} = \varepsilon\varepsilon_\alpha\vec{E} + \left(\frac{\sigma}{i\omega}\right)\vec{E} = \left(\varepsilon_\alpha\varepsilon + \frac{\sigma}{i\omega}\right)\vec{E} = \varepsilon\vec{E} \quad (22)$$

where ε is the complex dielectric constant. This equation completely explains the behavior of a dielectric material.

Thus it is evident that the electrical behavior of a dielectric medium can be sufficiently expressed by either of two complex parameters: the complex electrical permittivity or the electrical conductivity, the latter is given as:

$$\sigma^* = \frac{1}{\rho^*(\omega)} = i\omega\varepsilon_\alpha\varepsilon^*(\omega) \quad (23)$$

In this study, emphasis was placed on electrical conductivity to explore the mechanisms of strain sensing in metallic particulate reinforced cementitious systems. This is because of the ease of measuring frequency dependent conductivity both in the lab and the field, as well as the relative ease in interpretation of conductivity data.

4.2.2 Analytical Equations to Extract Fundamental Electrical Properties from Nyquist Plots

In cementitious composites, the electrical properties of the components are frequency dependent and thus, any efficient accurate numerical simulation of the electrical properties will need accurate frequency dependent electrical parameters as inputs to the model. The effective properties of such composite systems are a non-linear combination of individual properties due to its complex microstructure [40]–[42]. For the given metallic reinforced cementitious system, the microstructure can be considered to be composed of host (cement paste), inclusions (elongated iron powder), an interface between the inclusion and the matrix, and voids. Any simulation involving electrical properties of cementitious composites needs an accurate description of the electrical properties of the individual components. The electrical properties also depend on the

volume fraction, shape and size of the inclusions and their apparent location in the microstructure, which will be discussed later in the thesis.

Equations (24) – (43) given below were used to extract the frequency dependent conductivity and electrical permittivity of plain cement paste [43]. Most of the parameters used in the equations below have been explained in the earlier sections. The formulation for permittivity is presented first, followed by conductivity. This is because determination of the complex frequency dependent conductivity requires the separation of real and imaginary parts of the permittivity.

$$\varepsilon_m = \frac{1}{j\omega C_0 Z} \tag{24}$$

$$\varepsilon_m = \frac{1}{j\omega C_0 (Z' - Z'')} \tag{25}$$

$$\varepsilon_m = \frac{1}{j\omega C_0 Z' - j^2 \omega C_o Z''} \tag{26}$$

$$\varepsilon_m = \frac{1}{j\omega C_0 Z' + \omega C_o Z''} \tag{27}$$

Now, $\varepsilon_m = \varepsilon' - j\varepsilon''$

$$\varepsilon' - j\varepsilon'' = \frac{1}{\omega C_0 Z'' + j\omega C_o Z'} \tag{28}$$

Using the properties of complex numbers, RHS of Equation 28 can be expressed as:

$$= \frac{\omega C_0 Z'' - j\omega C_o Z'}{(\omega C_0 Z'' + j\omega C_o Z')(\omega C_0 Z'' - j\omega C_o Z')} \tag{29}$$

$$= \frac{\omega C_0 Z'' - j\omega C_o Z'}{(\omega C_0 Z'')^2 + (\omega C_o Z')^2} \tag{30}$$

$$= \frac{\omega C_0 Z'' - j\omega C_o Z'}{\omega^2 C_0^2 (Z'^2 + Z''^2)} \tag{31}$$

$$\varepsilon' - j\varepsilon'' = \frac{\omega C_0 Z''}{\omega^2 C_0^2 (Z'^2 + Z''^2)} - \frac{j\omega C_o Z'}{\omega^2 C_0^2 (Z'^2 + Z''^2)} \tag{32}$$

By comparing LHS and RHS we have,

$$\varepsilon' = \frac{\omega C_0 Z''}{\omega^2 C_0^2 (Z'^2 + Z''^2)} \tag{33}$$

and

$$\varepsilon'' = \frac{\omega C_o Z'}{\omega^2 C_0^2 (Z'^2 + Z''^2)} \tag{34}$$

Thus,

$$\varepsilon' = \frac{Z''}{\omega C_0 (Z'^2 + Z''^2)} \tag{35}$$

$$\varepsilon'' = \frac{Z'}{\omega C_0 (Z'^2 + Z''^2)} \tag{36}$$

where,

$$C_o = \frac{\varepsilon_0 A}{d} \tag{37}$$

Conductivity can be represented as:

$$\sigma(\omega) = \varepsilon'' \omega \varepsilon(\omega) \tag{38}$$

$$\sigma(\omega) = \frac{Z' \omega \varepsilon(\omega)}{\omega C_0 (Z'^2 + Z''^2)} \tag{39}$$

$$\sigma(\omega) = \frac{Z' \omega}{\omega C_0 (Z'^2 + Z''^2)} \left[\frac{Z''}{\omega C_0 (Z'^2 + Z''^2)} - \frac{jZ'}{\omega C_0 (Z'^2 + Z''^2)} \right] \tag{40}$$

$$\sigma' - j\sigma'' = \frac{Z' \omega}{\omega C_0 (Z'^2 + Z''^2)} \left[\frac{Z''}{\omega C_0 (Z'^2 + Z''^2)} - \frac{jZ'}{\omega C_0 (Z'^2 + Z''^2)} \right] \tag{41}$$

So $\sigma' = \frac{Z'' Z' \omega}{\omega^2 C_0^2 (Z'^2 + Z''^2)^2}$ (42)

And

$$\sigma'' = \frac{Z'^2 \omega}{\omega^2 C_0^2 (Z'^2 + Z''^2)^2} \tag{43}$$

where Z = Z'+Z'' with Z' being the real part of the impedance and Z'' being the imaginary part of the impedance, ω is the angular frequency represented by 2πf, σ(ω)

=σ'(ω)+σ''(ω) with σ' is the real conductivity and σ'' is the imaginary part of the conductivity, ε(ω) =ε'(ω)+ε"(ω) with ε' is the real permittivity and ε" is the imaginary part of the permittivity, ε_0 is the permittivity of free space or vacuum (8.85 x 10^{-12} F/m), A is the cross-section area of the electrodes, and L is the length of the sample.

4.2.3 Electrical Conductivity and Electrical Permittivity of Host (Cement Paste)

The impedance data of the cement paste sample was used to calculate the frequency dependent electrical permittivity and electrical conductivity of the host using Equations (24) to (43) and are presented in Figures 25 and 26. To fit the experimental electrical permittivity, a classic Cole-Cole dispersion equation [44] was used. The Cole-Cole model considers that the frequency dependence of electrical permittivity consists of a constant value at low frequencies to a small value at higher frequencies which is due to the polarization of the medium. They developed their equation from the classical Debye equation of dispersion in dielectrics, given as:

$$\varepsilon^* - \varepsilon_\infty = \frac{(\varepsilon_0 - \varepsilon_\infty)}{(1 + i\omega\tau_0)} \tag{44}$$

where, ε* = complex permittivity, ε_∞ = permittivity at large or infinite frequency, ε_0 = permittivity at lower frequency and τ_0 = relaxation time for the static dielectric constant. Cole-Cole modification of the Debye equation which accounted for different relaxation processes, using a dispersion parameter 's', is shown in Equation 45.

$$\varepsilon^* - \varepsilon_\infty = \frac{(\varepsilon_0 - \varepsilon_\infty)}{1 + (i\omega\tau_0)^{1-s}} \tag{45}$$

It can be observed from Equation (45) that the Cole-Cole equation reduces to Debye equation for s=0 and the dispersive region is increased by increasing the 's' value. Debye model can be characterized as a simplified model with single relaxation time whereas CCM (Cole-Cole Model) utilizes a distribution of the time constants to incorporate the effect of different phases by varying the value of (1-s). When (1-s) decreases, the relaxation time peak becomes broader whereas when (1-s) increases, peaks become narrower. Mathematically, CCM can be represented as the superimposition of multiple Debye relaxation process with a probability distribution F(τ) [44], [45] as:

$$\varepsilon^* = \varepsilon_\infty + \int_0^\infty \frac{F(\tau)}{1+i\omega\tau} d\tau \quad (46)$$

where,

$$F(x) = \frac{1}{2\pi} \frac{\sin(\alpha\pi)}{\cosh[(1-\alpha).x]-\cos(\alpha\pi)}, \; x=\ln(\tau/\tau_0) \quad (47)$$

Here, τ_0 is the geometric mean of the distribution, F(τ).

Generally, the parameter 's' and the time constant *(τ)* are used as tuning parameters to fit the experimental trends. Although there are different types of polarization, Cole-Cole equation is more efficient in characterizing the more fundamental dispersion form and thus, was used to fit the experimental permittivity data as shown in Figure 25.

There is no general method to calculate the time constant but the initial estimate can be made by employing the frequency where the experimental permittivity starts approaching a constant value. Then, it can be iterated to fit the experimental results. For a dielectric material such as concrete, s value is adopted in the range of (0.8-0.99) [37,45,46]. For this fit, s was taken as 0.99 and time constant was taken as 0.01 s.

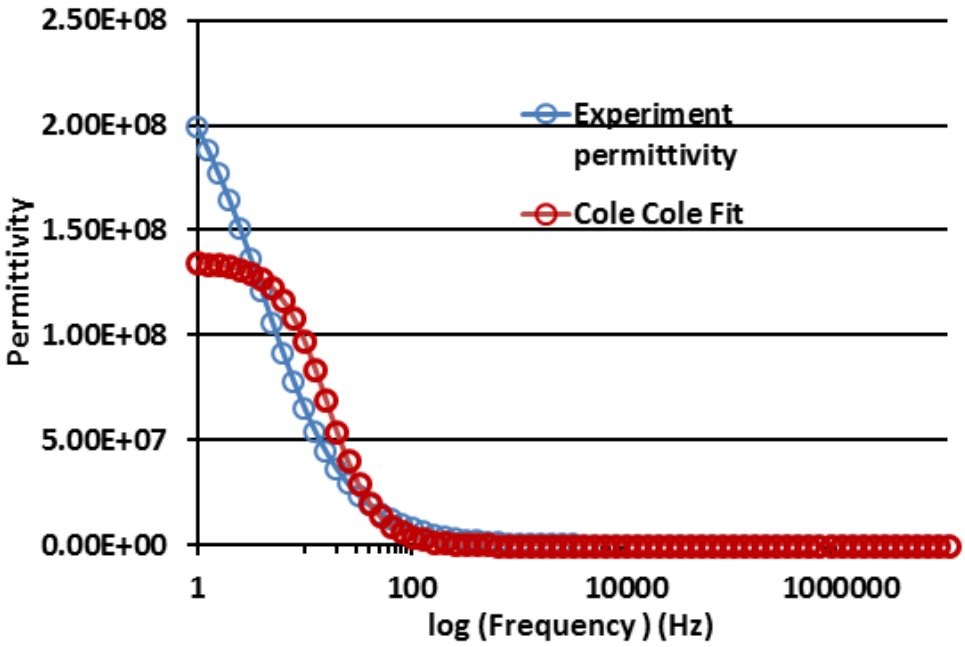

Figure 25: Complex permittivity and Cole-Cole equation fit for a plain cement paste

Similar to electrical permittivity, frequency dependent electrical conductivity was also extracted from the impedance data using Equations (24) to (43). It can be observed from Figure 26 that at a higher frequency, the conductivity also approaches a constant value due to the relaxation of the polarization mechanism in the dielectric (cement paste matrix). To fit the electrical conductivity data, a modified Cole-Cole model developed by Tarasov and Titov [46] was used. Tarasov and Titov analyzed the Cole-Cole and Pelton equation simultaneously and developed their equation using the electrical conductivity at higher frequencies and the polarization magnitude (chargeability) as given below:

$$\sigma_{CC}^{*} = \sigma(\infty)\left[1 - \frac{m}{1+(i\omega\tau)^{c}}\right] \tag{48}$$

where, $m = (\sigma_{\infty} - \sigma_{0})/\sigma_{\infty}$ is the chargeability. τ and c are generally used as tuning parameters in the above equation to fit the data. For the fit given below, m = 0.99, c = 0.8

and time constant τ = 0.01 sec. The electrical permittivity and conductivity equations obtained after fitting are used as inputs in the coupled electro-mechanical FE model explained in the following chapter.

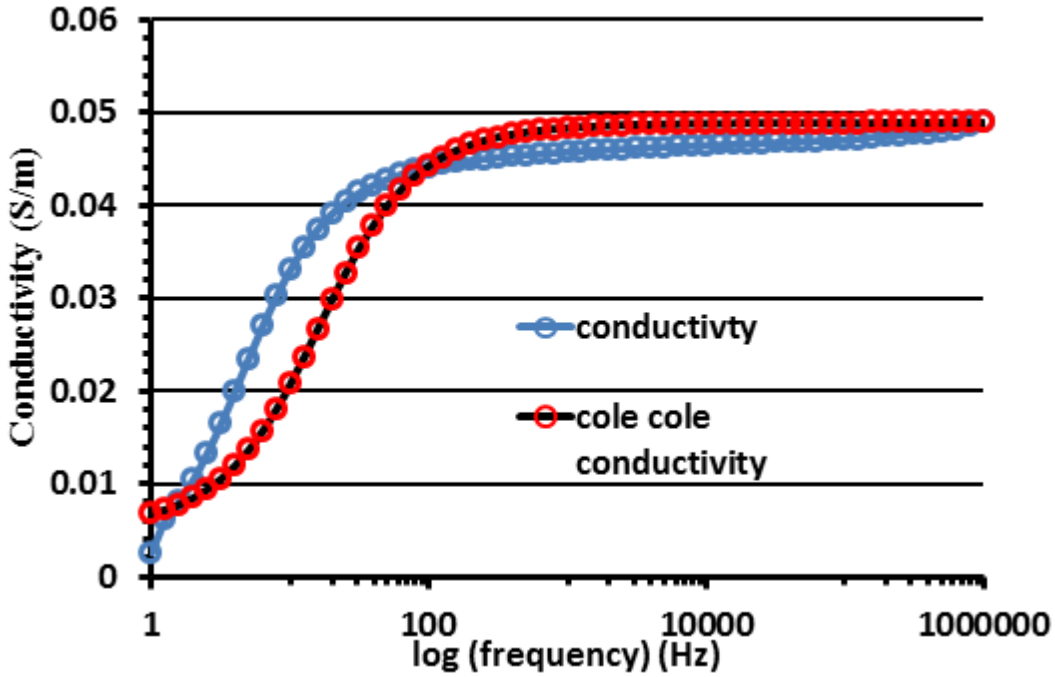

Figure 26: Complex conductivity and Cole-Cole conductivity equation fit for a plain cement paste

4.2.4 Electrical Conductivity and Electrical Permittivity of Inclusions (Iron Powder)

The mode of conduction in metals (iron) is via electrons, whereas in dielectrics it is usually ionic. The permittivity of metals such as iron is not readily measured as the polarization effect is usually overshadowed by the conduction. The electrons are free to move in a metal with relative ease and as the direction of potential is changed in an alternating current, electrons can easily change the direction and negate out the entire field inside the metal.

Thus, for all practical purposes, the conductivity and relative permittivity of metals such as iron are frequency independent unless high frequencies such as 10^{10} Hz or higher is applied. At such higher frequencies, the rate of change of direction of frequency is so high that the electrons just oscillate around the same position. But the frequency applied in this study is in the range of 10 Hz to 10^6 Hz and thus, constant electrical conductivity and permittivity can be safely assumed [42]. The electrical conductivity of the inclusion was taken as 100 S/m and the relative permittivity as 3 [48], [49].

4.2.5 Electrical Conductivity and Electrical Permittivity of Voids

In the generated microstructure, voids are representative of pores in a real cementitious matrix which shows a wide dispersion in sizes [23]. The size range of pores is important as they act as a connecting pathway when saturated with water. The pore solution contains many different ions including Cl^- , Mg^{2+}, and Na^+ and hence the pores can conduct electricity. The electrical conductivity of the voids adopted is in the range of (8-11 S/m) because of the presence of conductive pore solution, as reported in the literature [26, 47]. The relative permittivity of the voids with the pore solution is taken as 40.

4.2.6 Electrical Conductivity and Electrical Permittivity of the Interface

Previous literature [48, 49] have reported that interfacial zones exist between conducting particles and the insulating matrix in metallic reinforced composite. The interface (whether it is an aggregate-matrix interface or an inclusion-matrix interface) is a weak zone in the cement paste due to a higher porosity of the interface when compared to the bulk matrix. This is due to formation of larger crystals of hydration product and preferential deposition of calcium hydroxide crystals at the interface [53]. Theoretically, the electrical conductivity and permittivity of the interface should be higher than the bulk

cement matrix due to higher porosity and water saturation. The interfacial zones can also form connecting pathways even before the actual inclusion can physically form a conducting path and thus they influence the electrical properties of the matrix [45]. In this study, the conducting particles are assumed to be surrounded by an interface of constant thickness and the electrical properties of the interface were calculated in accordance with the methodology developed by Cai and Tu (2005) [54]. The inclusion and interface is combined into an 'effective particle' in this formulation. The conductivity of the interface was calculated using the following set of equations.

$$\phi_e = \frac{\phi}{\upsilon} \tag{49}$$

$$\upsilon = \frac{ab^2}{(a+\lambda)(b+\lambda)^2} \tag{50}$$

$$3(1-\upsilon)\frac{\sigma_2 - \sigma_i}{\sigma_i} + \upsilon\left(\frac{\sigma_2 - \sigma_p}{\sigma_i + A_{p1}(\sigma_p - \sigma_i)} + \frac{4(\sigma_2 - \sigma_p)}{2\sigma_i + (1-A_{p1})(\sigma_p - \sigma_i)}\right) = 0 \tag{51}$$

$$9(1-\phi_e)\frac{\sigma_1^{\frac{1}{s}} - \sigma_{eff}^{\frac{1}{s}}}{2\sigma_{eff}^{\frac{1}{s}} + \sigma_1^{\frac{1}{s}}} + \phi_e\left(\frac{\sigma_2^{\frac{1}{t}} - \sigma_{eff}^{\frac{1}{t}}}{\sigma_{eff}^{\frac{1}{t}} + A_{21}\left(\sigma_2^{\frac{1}{t}} - \sigma_{eff}^{\frac{1}{t}}\right)} + 4\frac{\sigma_2^{\frac{1}{t}} - \sigma_{eff}^{\frac{1}{t}}}{2\sigma_{eff}^{\frac{1}{t}} + (1-A_{21})\left(\sigma_2^{\frac{1}{t}} - \sigma_{eff}^{\frac{1}{t}}\right)}\right) = 0 \tag{52}$$

where, s =0.87 and t = 2.0 are numerical fitting parameters, σ_2 is the conductivity of the effective particle, σ_i is the conductivity of the interface, σ_p is the conductivity of the inclusion, σ_1 is the conductivity of the matrix, ϕ_e is the volume fraction of the effective particles, σ_{eff} is the conductivity of the composite, a and b are the length of semi-axis of the inclusion particle (a = b for a circular inclusion), and ϕ is the actual volume fraction of inclusion. $A_{11} = A_{12} = A_{13} = 1/3$ are the depolarization factors, $R_{eff} = (a+\lambda)/(b+\lambda)$ and $A_{2,1} = 1/3$ for $R_{eff} = 1$, λ is the effective thickness of interface.

This methodology was programmed in MATLAB to back-calculate the interfacial properties. Figure 27 presents the back-calculated frequency dependent electrical conductivity of the interface. The thickness of the interface is taken as 5 μm. While it is conceivable that the interface thickness varies with inclusion and matrix types, such a consideration was not made in this thesis for ease of analysis. The MATLAB formulation is presented in the appendix. After back-calculating the electrical properties, the Cole-Cole model (described earlier for both permittivity and conductivity calculations) was again used to fit the experimental value (Figures 27 and 28). These Figures show that this approach is efficient in obtaining frequency dependent electrical properties of the interface. For electrical conductivity fit, m is taken as 0.99, time constant is taken as 8.6 x 10^{-3} s and value of c is 0.4. For electrical permittivity fit, s is taken as 0.99, time constant is taken as 8.6 x 10^{-3} s and m is taken as 0.99. These parameters have been described earlier.

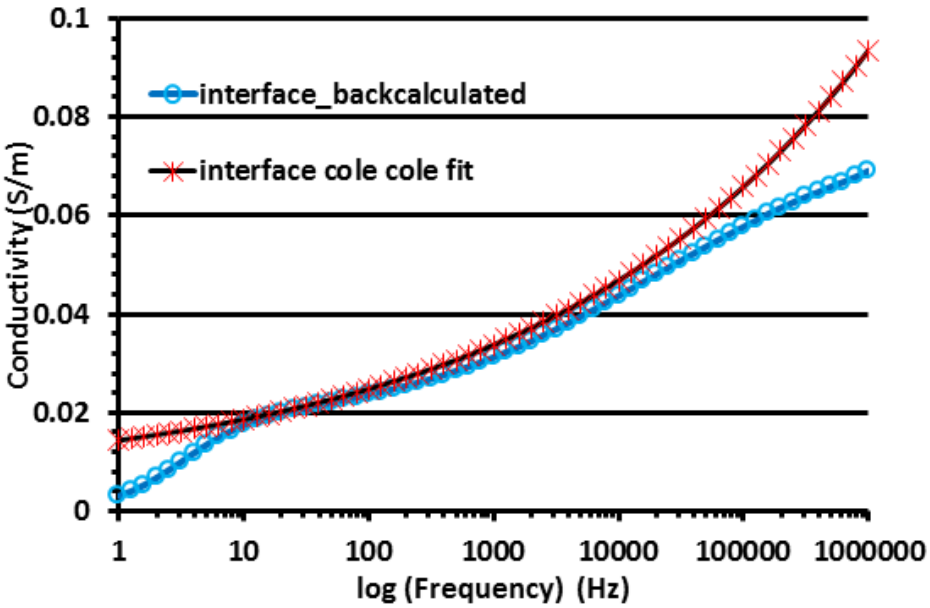

Figure 27: Back-calculated complex conductivity and Cole-Cole equation fit for interface

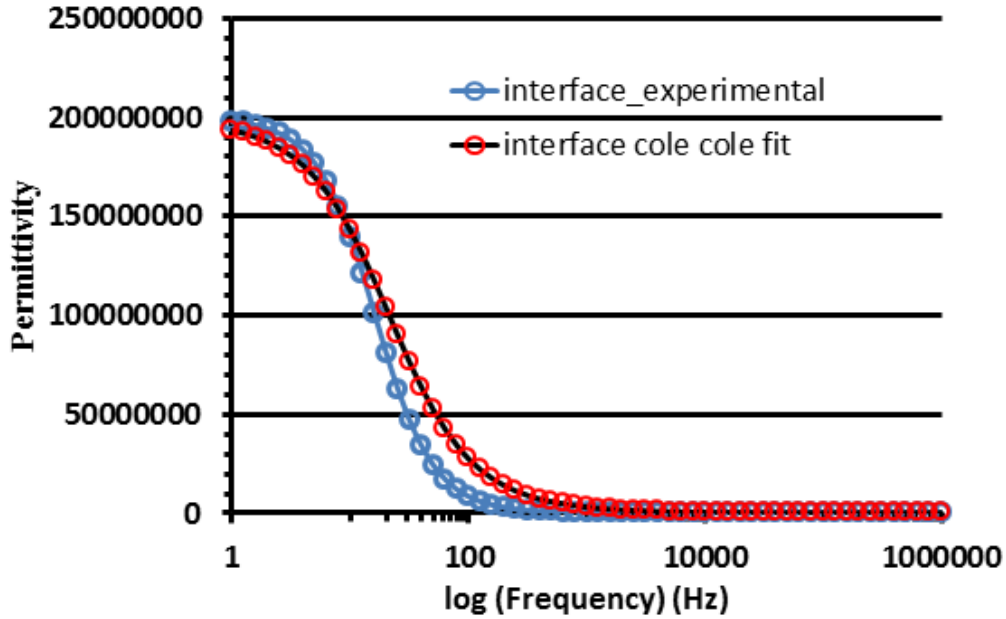

Figure 28: Back-calculated complex permittivity and fit using Cole-Cole conductivity equation for interface

4.3 Evaluating Shape and Orientation Effects of Inclusions on Electrical Properties of Composites

A study on the effect of shape and orientation of inclusions on the electrical properties was conducted and is reported in this section. Some of the important factors that influence the electrical properties of the composite are the material microstructure, volume fraction, shape and size of inclusions and their relative placement with respect to each other in the matrix. Thus, this simulation attempts to help develop the guidelines to create the algorithm for generation of microstructure with multiple inclusions as well as to understand the geometric parameters that are needed for the simulation.

4.3.1 RVE with Circular Inclusions

A representative volume element (RVE) of 200 μm x 200 μm was adopted with an inclusion radius of 20 μm and interface thickness of 5 μm. Details of microstructure generation are included in Chapter 5 since that chapter describes a more involved process of creating multi-phase microstructures. In summary, size of the inclusion and the volume fraction of inclusion are provided as inputs to COMSOL. A MATLAB link is used to create the interface. The positioning of particles is randomized. Please see Chapter 5 for more details. The electrical property modeling was also done in a COMSOL environment. The electrical properties needed for simulation (for paste, inclusion, and the interface) were obtained as described earlier in this chapter.

A potential of 1 V was applied as the boundary condition to the RVE. The boundary conditions included ‘electric potential’ on the top face which provides an electric potential of 1 V, ‘insulation’ (the default boundary condition which follows n.J =0) for the left and the right faces and ‘ground’ for the bottom face which implies a zero

potential (V = 0). After the simulation, the surface average of current density and electric field in the y-direction was calculated, and conductivity was derived as follows:

$$\sigma = \frac{<J>}{<E>} \tag{53}$$

where, σ is the complex conductivity, J is the surface average of current density in y-direction and E is the surface average of electric field in y-direction. Figures 29-31 show the derived electrical properties for an RVE with circular inclusions, which includes current density, electric field, and electric potential. The averaged current density and electric field is used to determine the averaged RVE conductivity. The simulation was carried out for several different frequencies and the results are tabulated in Table 6. As can be noticed from the results, the real part of the composite conductivity slightly increases with frequency.

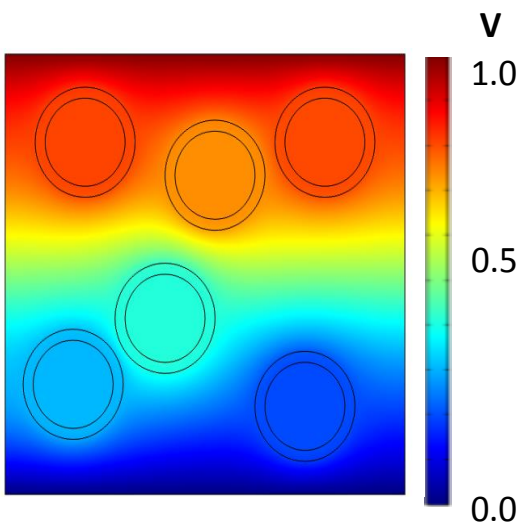

Figure 29 : Electrical potential distribution in the RVE containing circular inclusions, simulated at a frequency of 1000 Hz

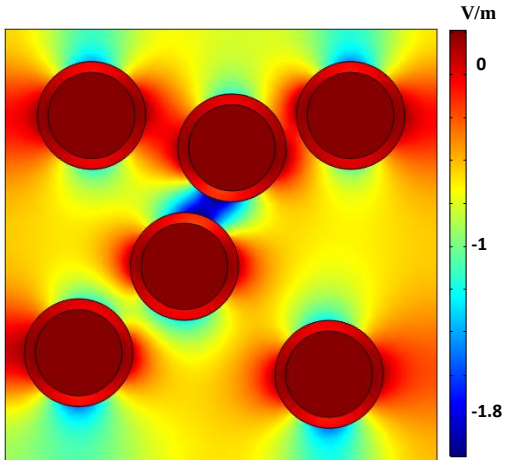

Figure 30: Electric field distribution in the RVE containing circular inclusions, simulated at a frequency of 1000 Hz

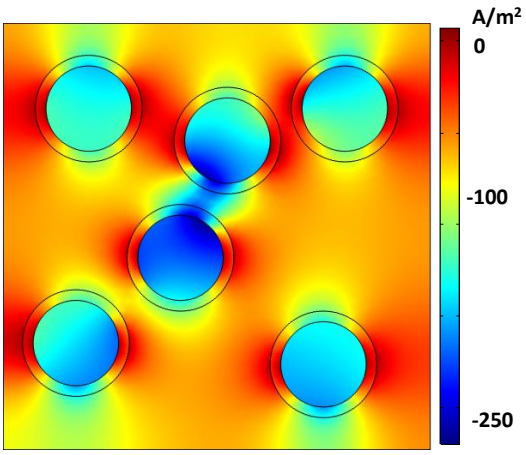

Figure 31: Current density distribution in the RVE containing circular inclusions, simulated at a frequency of 1000 Hz

Table 6: Electrical conductivity of RVEs containing circular inclusions

Circular Inclusions				
Frequency (Hz)	J (A/m^2)	E (V/m)	Complex conductivity(S/m)	Real part (S/m)
100	-108.66-19.826i	-5000	0.0217+0.0039i	0.0217
500	-114.37-5.784i	-5000	0.0229+0.0011i	0.0229
1000	-115.37-3.8018i	-5000	0.02314+0.0007i	0.0231
10000	-116.86-1.945i	-5000	0.0234+0.0004i	0.0234
100000	-119.26-2.5667i	-5000	0.0238+0.0005i	0.0238
1000000	-121.68-10.733i	-5000	0.0243+0.0002i	0.0243

4.3.2 RVE with Elliptical Inclusions

Similar RVEs of 200 μm x 200 μm were generated, this time containing elliptical inclusions having an aspect ratio of 2.0. The total surface area and the volume fraction of the inclusions were kept constant for both circular and elliptical inclusions. Figures 32-34 show the electrical properties for an RVE with elliptical inclusions, derived from the simulations. The simulation was carried out for several different frequencies and the results are tabulated in Table 7.

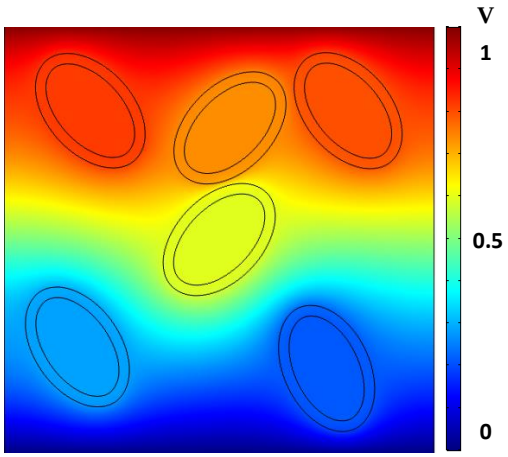

Figure 32: Electrical potential distribution in the RVE containing circular inclusions simulated at a frequency of 1000 Hz

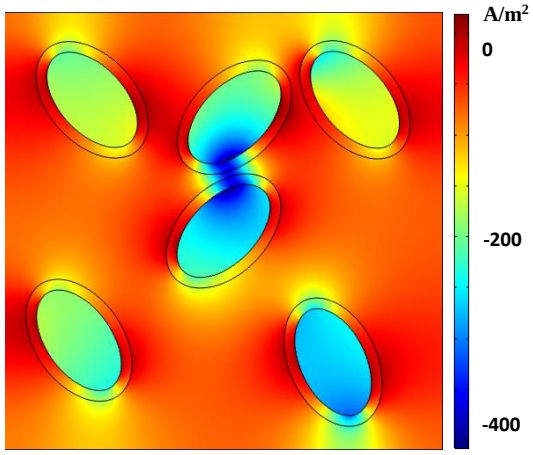

Figure 33: Current density distribution in the RVE containing elliptical inclusion simulated at a frequency of 1000 Hz

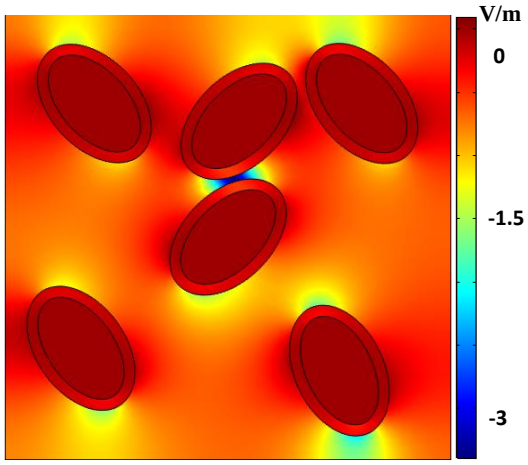

Figure 34: Electric field distribution in the RVE containing elliptical inclusion simulated at a frequency of 1000 Hz

Table 7: Electrical conductivity of RVEs containing elliptical inclusions

Elliptical inclusions				
Frequency(Hz)	J (A/m^2)	E (V/m)	Complex conductivity (S/m)	Real part (S/m)
100	-117.32-21.459i	-5000	0.0235+0.0043i	0.0235
500	-123.51-6.2669i	-5000	0.0247+0.0012i	0.0247
1000	-124.6-4.121i	-5000	0.0251+0.0008i	0.0251
10000	-127.41-2.1294i	-5000	0.0254+0.0004i	0.0254
100000	-130.02-2.7985i	-5000	0.0260+0.0005i	0.0260
1000000	-132.66-11.714i	-5000	0.0265+0.0002i	0.0265

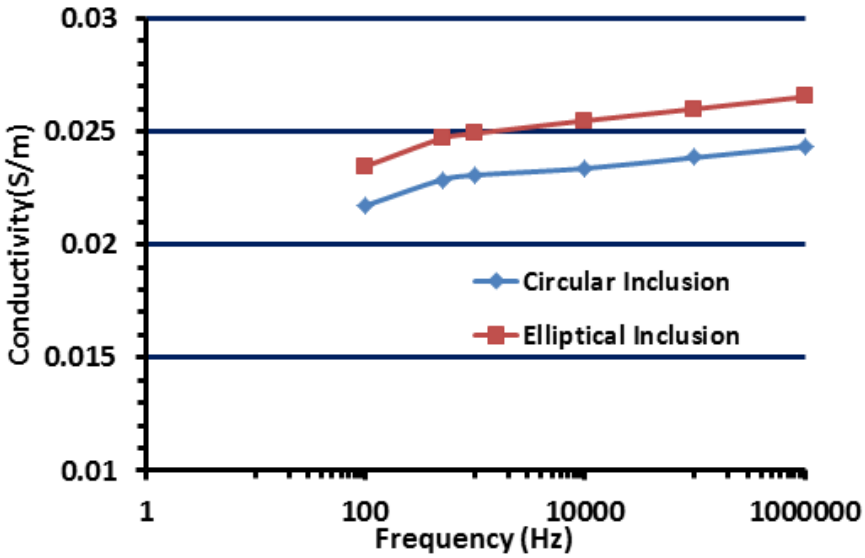

Figure 35: Real part of complex conductivity of the RVE with circular and elliptical inclusions as a function of frequency

Figure 35 shows the change in electrical conductivity as a function of frequency for the RVEs containing circular and elliptical inclusions. Note that the volume fractions of all the phases are the same in both the cases. It is evident from Figure 35 that the electrical conductivity of the RVE with elliptical inclusions is slightly higher when compared to RVE with circular inclusion. This can be attributed to the higher surface area of the ellipse as compared to the circle for the same volume fraction. Since the inclusions are more conductive than the host in the scenarios considered in this study, this result is expected. The increase in overall electrical conducting paths in the microstructure, no doubt, increases the conductivities [52]. This simulation also shows that the trends in frequency dependent conductivities are invariant with inclusion shapes. However, when the aspect ratio of ellipse becomes higher (to simulate fiber-like particles), this trend might not remain exactly the same. In any case, the simulations provide a rationale to use

circular particles to simulate conductive inclusions in this study, since the computational time is less with circular inclusions. Hence, circular inclusions are used for all simulations described in Chapter 5.

Chapter 5: Modelling the Strain Sensing Response through Coupled Electro-Mechanical Modeling

This chapter outlines the general procedure adopted for the coupled electro-mechanical finite element (FE) model for strain sensing response of conductive particulate composites. The general setup of the model is discussed in this chapter. The electrical input parameters for different components derived in the chapter 4 are used here to carry out the simulations.

The simulation in COMSOL can be divided into three distinct steps:

1. Creation of geometry;
2. Assigning the material properties depending upon the physics of the problem, defining mesh sizes, mesh generation, and assigning the multi-physics study type; and
3. Solving the model to determine the electrical parameters.

5.1 Microstructure Generation

The metallic particulate reinforced cementitious system has a complex microstructure but COMSOL can only generate simple microstructures. COMSOL has a dedicated MATLAB (known as LiveLinkForMATLAB) interface which can be used to generate the desired microstructure. This is used in this thesis. The basic code and the modification adopted are also documented in the appendix. The following steps highlight the methodology adopted to generate the microstructure:

1. In this particular program, the size of the representative element, the minimum and the maximum size of the inclusion and the volume fraction of inclusions are provided

as inputs. For this particular simulation, the size of a representative element was selected to be 200 μm x 200 μm. The size of inclusion particle was chosen as 21 μm.

2. The program commences by attempting to generate the center coordinates of the first particle. A random number is selected within the bounds of representative element size and is designated as the center coordinates of the first particle. A variable 'ratio' is used to keep track of the volume fractions of inclusions.
3. The random number selected is further adjusted by adding a constant to the coordinates, which gives a threshold limit to particle size.
4. After a random number is generated, a loop is created to check whether the generated coordinates can create an inclusion that fits within the RVE. To achieve this, the radius of the inclusion is added and subtracted from the randomly generated numbers to create bounds of individual inclusion. Using the equation for a circle, it is also verified that all the positions generated lie within the RVE.
5. After verification, a variable is initialized to calculate the volume fraction generated. In this program, the variable, 'Area' is used which is incremented by a constant increment as soon as the position of one inclusion is generated and verified.
6. One of the disadvantages of several existing microstructure generation algorithms is that there is little to no control over the overlapping of the inclusions. For all practical purposes, the particles do overlap and coagulate in a cementitious matrix. But for the purpose of understanding the concept of percolation threshold and the effect of shape on the strain sensing, the program was developed such that no two particles overlap.
7. To achieve no overlapping, when next random position is selected, the number of available numbers to choose from is reduced and a threshold weight added. The

weight selected in this program was decided after multiple iterations. The procedure is applied to both X and Y coordinates.

8. Once again, the variable 'Area' is incremented to control the volume fraction generated. As it is a 2-D microstructure, the volume fraction is indicated by the area fraction.
9. After the position of the inclusion has been generated, it is stored in a vector and the microstructure is generated using these position vectors using the COMSOL Livelink.
10. COMSOL Live link has its own standard methodology to create geometric features which is then utilized to create the required geometry. The complete MATLAB code is provided in the appendix of the text.

Figure 36 shows the generated representative volume element for a cement mortar containing 20% iron powder replacing cement, and the interface and voids.

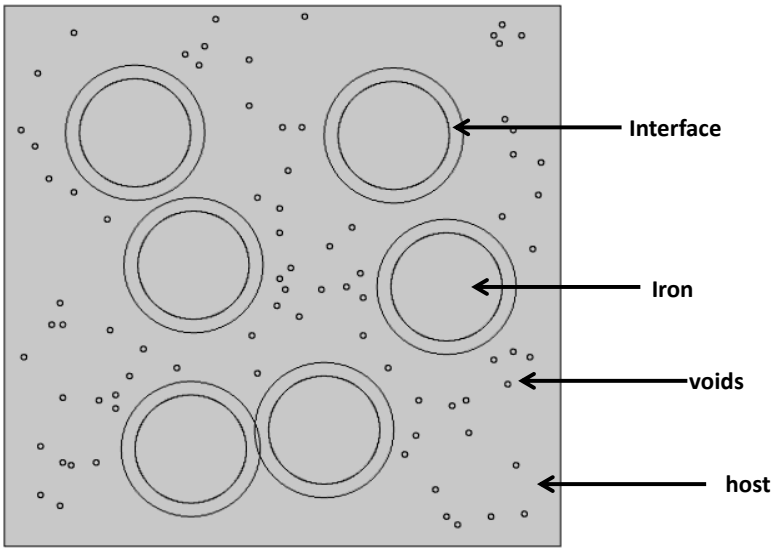

Figure 36: 200µm x 200µm RVE representing a system with 20% iron powder replacing OPC, along with the interface and voids

5.2 Coupled Electro-Mechanical FE Model

5.2.1 Model Formulation

The next step involved setting up of the physics modules in the required FE model. The following sequence was adopted: initially the load (stress) was applied and then the electrical impulse applied. The solid mechanics module was used for general simulation of stress analysis. The solid mechanics interface solves the Navier's equation for stresses and strains in the RVE [56]. A 2-D RVE is employed and the material is assumed to be isotropic. The elastic equations for displacement and subsequently, strains and stresses, for a linear elastic material are solved. The elastic material properties used as input parameters for the model are shown in Table 8 for all the microstructural phases.

In the RVE, the top face is assigned to the boundary condition of the 'boundary load' where the stress is specified, the left and right faces are kept 'free', and a 'fixed' boundary condition applied to the bottom face. The free boundary condition showed that there was no constraint at that face and no loads would be acting on that boundary. The fixed constraint ensured that the displacements are zero in all the directions, making the geometrical entity completely constrained.

Table 8: Input parameters for structural mechanics module of the model

Properties	Host	Interface	Inclusion	Voids (Pore solution)
Elastic modulus(E) (Pa)	20×10^9	12×10^9	150×10^9	0.001
Poisson ratio (υ)	0.2	0.24	0.4	0.4999
Density (kg/m^3)	2000	1500	7850	1000

For providing the electrical impulse, the electric current interface of COMSOL Multiphysics 5.2a was utilized, which solved a current conservation problem. Similar to solid mechanics, the 2D microstructural model was used for the simulations. It solved the Maxwell equation for current density, electric field and electric displacement field for the whole RVE (as shown in the previous chapter). A 2-D plane strain approximation is employed. The frequency dependent input parameters derived in chapter 4 are utilized. The electrical property inputs were obtained from those derived in the previous chapter.

5.2.2 Solving the Model

After the generation of desired microstructure and setting up the model, type of study to be conducted for both the physics module was selected. A 'stationary' study was selected for the structural mechanics module and a 'frequency dependent' study was selected for the electric current module. Stationary study is used when the field variables do not change over time. In structural mechanics, the applied stress is constant for a particular simulation and thus stationary study can be used. Frequency dependent study applies the voltage over a frequency range and is apt to study the frequency dependent electrical properties. After the simulation, the required calculations were performed

5.2.3 Calculation of Conductivity and Simulating the Strain Sensing Response

After the simulation, the conductivity was calculated using Equation (54). From the calculated conductivity, the bulk resistance of the sample was calculated using Equation (55).

$$\sigma = \frac{<J>}{<E>} \tag{54}$$

$$R_b = \frac{L}{\sigma A} \tag{55}$$

Here, σ is the conductivity (S/m), J is averaged current density in y-direction (A/m^2), E is averaged electric field in y-direction (V/m), L is the length of the specimen, R is the resistance, and A is the area of the cross-section of the specimen.

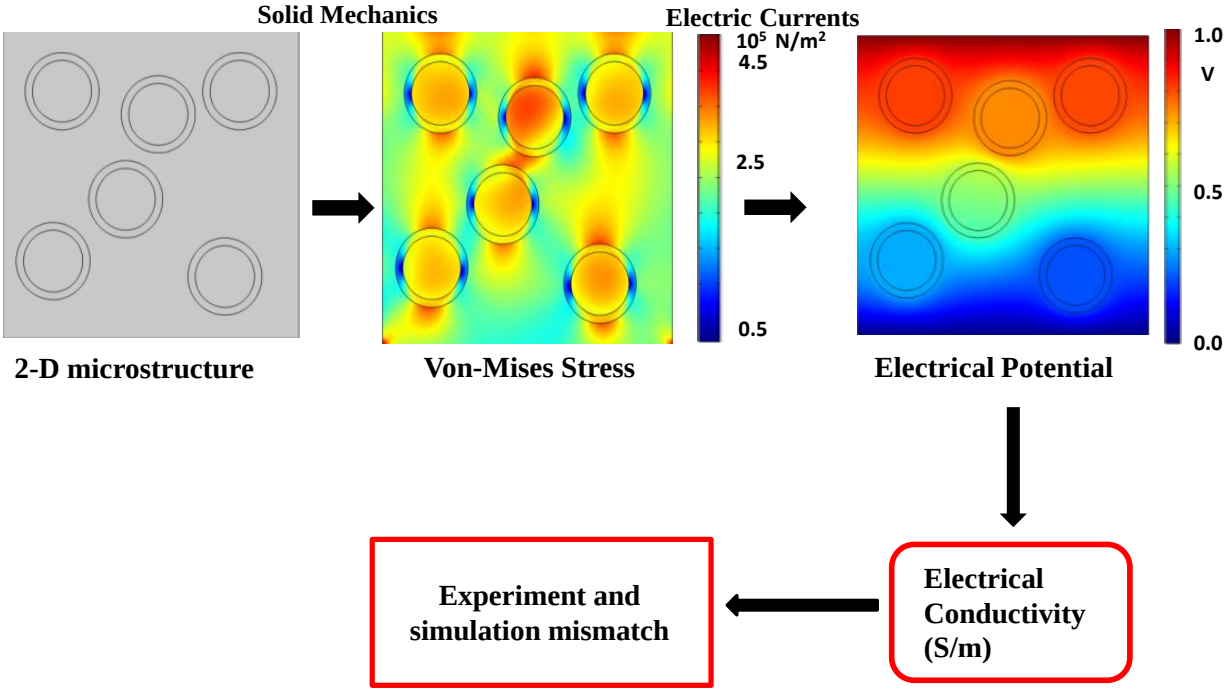

Figure 37: Generic schematics of coupled electro-mechanical model

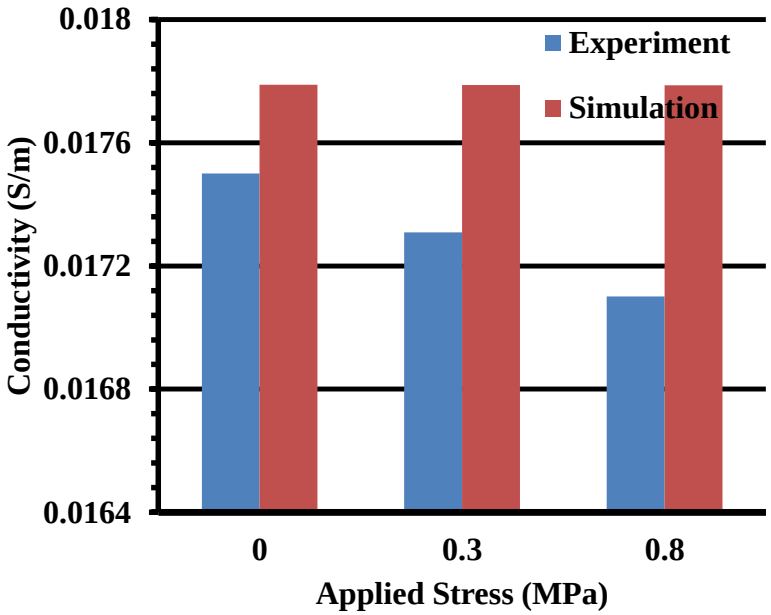

Figure 38: Experimental and predicted conductivities for cement mortar with 20% iron powder replacing OPC

Figure 37 shows the schematic of the coupled electro-mechanical model implementation. Figure 38 shows the experimental and predicted conductivities for different metallic particulate reinforced mortars, showing mismatch between the experiments and simulation values. As evident from the Figure 38, the current model was unable to capture the fractional change in resistance of the composite systems under load. Careful examination of the output from the solid mechanics model suggested that the absence of considerations of interfacial debonding in the model might be the cause of this discrepancy. Even at small loads, due to the large elastic modulus and Poisson's ratio mismatch of the host matrix and inclusions, there is possibility of slight debonding of the matrix-interface region. For electrical properties, even slight discontinuities influence the electrical field and the current density, thereby enhancing the likelihood of differences in predicted electrical response. Hence the following section considers the effect of interfacial debonding in the simulations.

5.2.4 Interfacial Debonding

As mentioned earlier, and from previous literature, electrical properties are highly sensitive to the presence of discontinuities [57]. This necessitated the need to account for the effect of interfacial debonding in the FE model.

The interface is one of the weakest zones in the composite and the interfacial debonding is one of the most important characteristics defining the strain sensing capability of the material. Hence, the required modification was done in the model to capture the effects of the interfacial debonding on the deformation response of metallic powder reinforced composites. The influence of debonding was captured using a common traction-separation law. The traction separation relationship is one of the most important features of cohesive zone modeling. A bilinear softening model introduced by Peterson (1981) [58] is used to evaluate debonding. Many cohesive zone models are based on a pre-defined debonding path and are represented in four stages [59], [60]:

1. The first stage is represented through a generic elastic behavior without separation. The material properties are assumed to be elastic.
2. Initiation of debonding is accounted for in the second stage. In the current model, debonding is considered to occur when the fracture initiation criterion for Mode I occur due to state of stress reaching the cohesive strength (concrete tensile strength). Contact pairs were defined at the intersection of interface and the inclusion. Fracture parameters given in Table 9 were defined for the contact pairs.
3. The third stage refers to the evolution of de-bonding guided by the cohesive law or the softening curve, i.e., relationship between the stress (σ) and crack opening width (w) across the debonded surfaces (Figure 39).

4. Stage 4 refers to the closing of the crack as the criteria specified in stage 2 are no longer met.

.

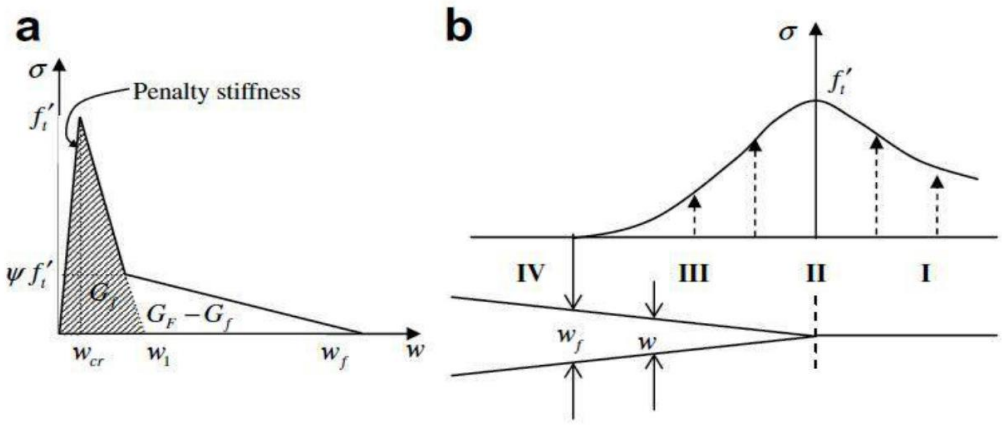

Figure 39: (a) Bilinear softening for quasi brittle materials and (b) four stages of the cohesive zone model

Some of the different constitutive relationships used to define interfacial debonding includes linear, bilinear, trilinear and exponential softening laws [58]–[61]. Bilinear softening model was utilized in this study due to the flexibility of controlling the slopes of the softening curve [62].The input parameters used for the traction-separation relationship used in the model are: tensile Strength (f'_t), tensile energy release rate (G_{IC}) and stress intensity factor(K_{IC}).

The values for the three parameters were adopted from literature [63], [64], and are shown in Table 9. Figure 40 shows the schematic of the modeling process, including the consideration of the effects of interfacial debonding.

Table 9: Input parameters for traction-separation relationship

f'_t	K_{IC}	G_{IC}
1.4 MPa	23 MPa$(mm)^{0.5}$	25 N/mm

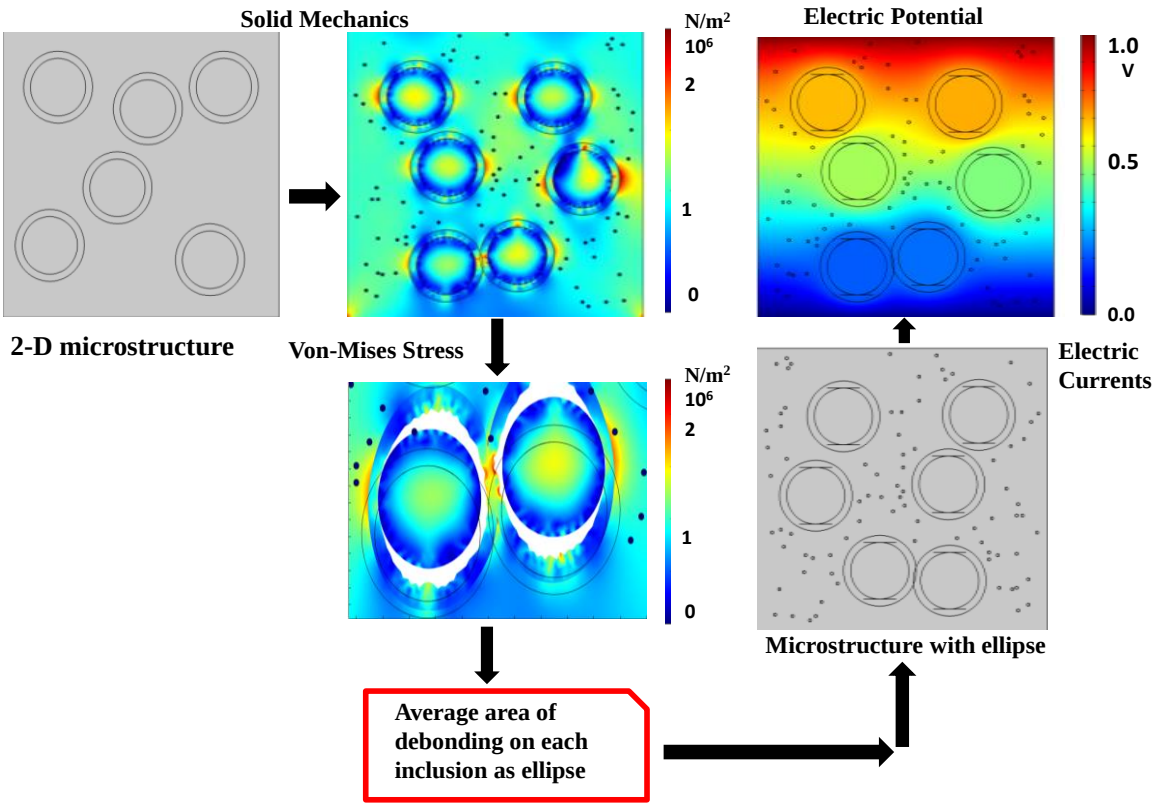

Figure 40: Schematics of the modified electro-mechanical coupled FE Model

5.2.5 Simplified Representation of Debonding

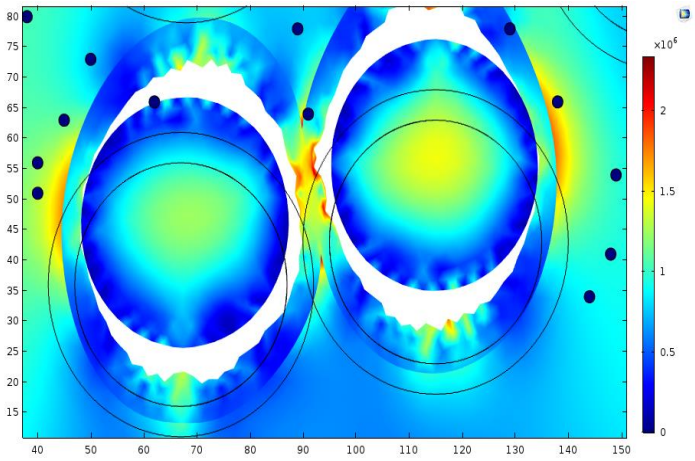

Figure 41: Debonding (magnified 5000X) around inclusion

Figure 41 shows a magnified view of the debonding around the inclusion. After the simulation, the average debonded area on each contact pair was averaged as COMSOL could not import the debonded geometry automatically. The area of debonding was represented as an ellipse on the top and bottom of the inclusion (at the inclusion-interface boundary). It was observed that for the stress range of 0.1 MPa to 0.8 MPa, the average debonding area varied between 0.022 μm^2 to 0.034 μm^2. The total debonding area varies with volume fraction of inclusions and their location in the real microstructure. For simplicity, in this analysis, the debonding area is assumed to be constant for all the inclusions. Figure 41 also indicates stress relaxation in the debonded zones and stress concentration in the partially debonded zones. Due to debonding, the interfacial surfaces are no longer in contact, thus impeding the stress transfer leading to stress relaxation. The stresses are then redistributed to the adjacent locations, leading to stress concentrations.

The debonded areas and the position of each inclusion (imported from the microstructure used in the solid mechanics module) were utilized to create a new geometry for the electric current analysis as shown in the schematic in Figure 40. Figures 42 and 43 show the current density and electric field distribution respectively on the debonded specimen.

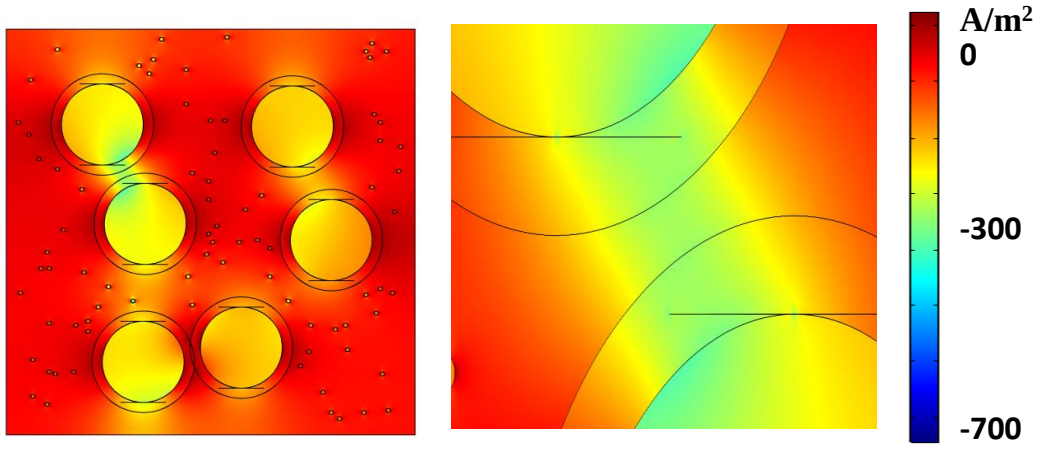

Figure 42: Current density distribution in the specimen with debonding represented as an elliptical area

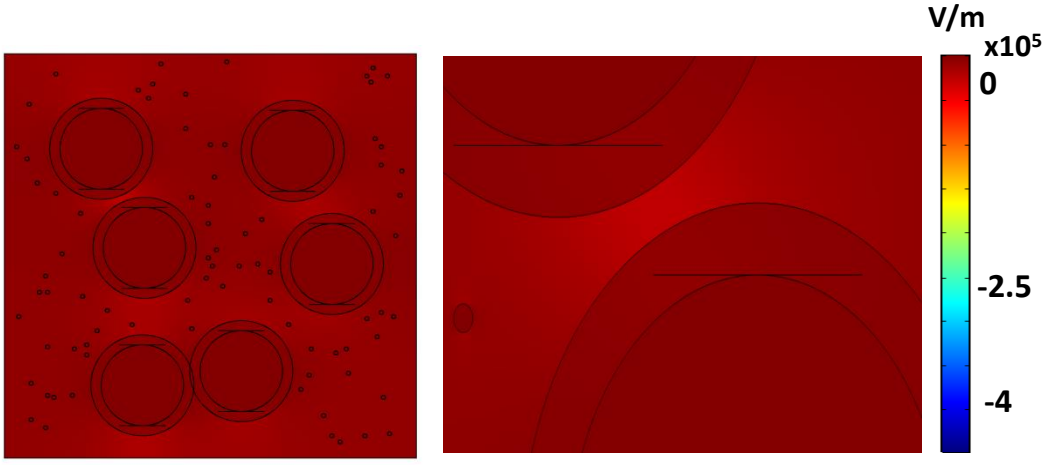

Figure 43: Electric field distribution in the specimen with debonding represented as an elliptical area

5.3 Results from Strain Sensing Simulations

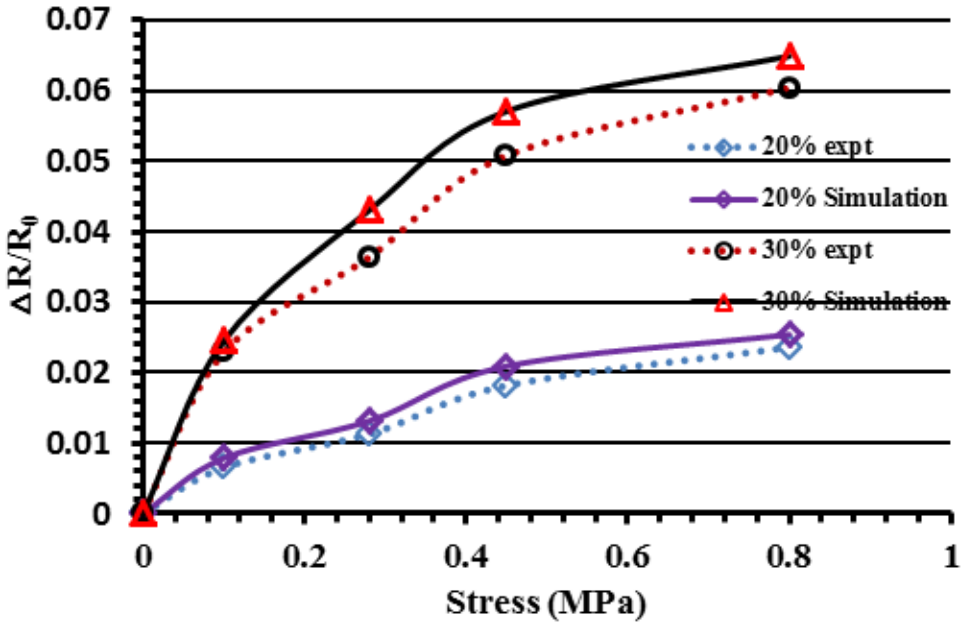

Figure 44: Experimental results and the simulation for $\Delta R/R_0$ vs stress for mortar containing 20% and 30% of iron powder replacing OPC

Figure 44 shows the experimentally obtained fractional change in resistance and those obtained from the electromechanical simulations as a function of stress for mortars with 20% and 30% of iron powder replacing OPC. The modified simulations are capable of matching the experimental fractional change in resistance well, attesting to the fact that a simplified representation of debonding is sufficient to explain the physical process in the system that influences electrical response. The simulation results also validate the methodology used in this work to extract the electrical parameters from simple analytical models. The difference between the experimental results and simulation values can be attributed to the simplified microstructure employed in this work. In experiments, the change in resistance with the application of stress is due to the weakening of the interface-inclusion bond and the changes in electrical path length [7, 15]. In the simulations, this weakening of the interface-inclusion bond and the subsequent

debonding is shown to be an important factor that accounts for the enhanced fractional change in resistance.

Chapter 6: Conclusions and Future Work

The following conclusions are arrived at from this research study.

1. Metallic powder reinforced cementitious composites are shown to be promising strain sensing materials. The fractional change in specimen resistance increased, with an increase in the applied load or stress. The efficiency of strain sensing was improved with increasing iron powder replacement percentage. Electrical circuit models were used to extract electrical parameters from the impedance spectroscopy data. The presence of conducting particles was found to amplify the strain sensing response.
2. The iron carbonate based binder was also shown to be a capable strain sensing material. Based on gage factors, it was found that the iron carbonate based binder was more efficient strain sensing material when compared to the metallic particulate reinforced cementitious composites. The added benefit is that iron carbonate can act as a strain sensing material without addition of any external conducting fibers due to the presence of unreacted iron particles in the matrix.
3. Using Maxwell equation, frequency dependent parameters were extracted for host (cement paste), interface, inclusion (iron) and voids to be used as input parameters into the generic model for coupled electro-mechanical behavior simulation. Cole-Cole spectral distribution equations for electrical permittivity and electrical conductivity were used to fit the experimental electrical permittivity and conductivity values. The effect of inclusion shape on the electrical conductivity was also evaluated.
4. The coupled electro-mechanical model was implemented in a COMSOL-MATLAB framework, considering the effects of interfacial debonding under stress, on the electrical conductivity. The developed model was able to accurately predict the trends

in fractional change in resistance, thereby providing a generic methodology to model the strain sensing response of conductive particulate and fiber reinforced cementitious matrices.

Future work will focus on the development of the model with higher aspect ratio of the inclusion so as to mimic the true shape of the iron powder. Also, the model developed would be extended to simulate the strain sensing behavior of iron carbonate.

REFRENCES

[1] "ASCE's 2017 Infrastructure Report Card | GPA: D+," *ASCE's 2017 Infrastructure Report Card*. [Online]. Available: http://www.infrastructurereportcard.org. [Accessed: 05-May-2017].

[2] S. Kim, J. Kang, S.-H. Lee, and Y. H. Ahn, "Effect of Chlorides on Conductivity and Dielectric Constant in Hardened Cement Mortar: NDT for Durability Evaluation," *Adv. Mater. Sci. Eng.*, vol. 2016, p. e6018476, May 2016.

[3] B.-J. Kim, C. Yi, and Y. Ahn, "Effect of embedment length on pullout behavior of amorphous steel fiber in Portland cement composites," *Constr. Build. Mater.*, vol. 143, pp. 83–91, Jul. 2017.

[4] E. Teomete, "Transverse strain sensitivity of steel fiber reinforced cement composites tested by compression and split tensile tests," *Constr. Build. Mater.*, vol. 55, pp. 136–145, Mar. 2014.`

[5] H. Y. Kordkheili, S. E. Shehni, and G. Niyatzade, "Effect of carbon nanotube on physical and mechanical properties of natural fiber/glass fiber/cement composites," *J. For. Res.*, vol. 26, no. 1, pp. 247–251, Mar. 2015.

[6] S. Wen and D. D. L. Chung, "Carbon fiber-reinforced cement as a strain-sensing coating," *Cem. Concr. Res.*, vol. 31, no. 4, pp. 665–667, Apr. 2001.

[7] P.-W. Chen and D. D. L. Chung, "Concrete as a new strain/stress sensor," *Compos. Part B Eng.*, vol. 27, no. 1, pp. 11–23, Jan. 1996.

[8] S. Wen and D. D. L. Chung, "Partial replacement of carbon fiber by carbon black in multifunctional cement–matrix composites," *Carbon*, vol. 45, no. 3, pp. 505–513, Mar. 2007.

[9] X. Shu, R. K. Graham, B. Huang, and E. G. Burdette, "Hybrid effects of carbon fibers on mechanical properties of Portland cement mortar," *Mater. Des. 1980-2015*, vol. 65, pp. 1222–1228, Jan. 2015.

[10] S. Xu, J. Liu, and Q. Li, "Mechanical properties and microstructure of multi-walled carbon nanotube-reinforced cement paste," *Constr. Build. Mater.*, vol. 76, pp. 16–23, Feb. 2015.

[11] O. Galao, F. J. Baeza, E. Zornoza, and P. Garcés, “Strain and damage sensing properties on multifunctional cement composites with CNF admixture,” *Cem. Concr. Compos.*, vol. 46, pp. 90–98, Feb. 2014.

[12] F. Azhari and N. Banthia, “Cement-based sensors with carbon fibers and carbon nanotubes for piezoresistive sensing,” *Cem. Concr. Compos.*, vol. 34, no. 7, pp. 866–873, Aug. 2012.

[13] D.-Y. Yoo, H.-O. Shin, J.-M. Yang, and Y.-S. Yoon, “Material and bond properties of ultra high performance fiber reinforced concrete with micro steel fibers,” *Compos. Part B Eng.*, vol. 58, pp. 122–133, Mar. 2014.

[14] S. Wen and D. D. L. Chung, “The role of electronic and ionic conduction in the electrical conductivity of carbon fiber reinforced cement,” *Carbon*, vol. 44, no. 11, pp. 2130–2138, Sep. 2006.

[15] P.-W. Chen and D. D. L. Chung, “Carbon fiber reinforced concrete for smart structures capable of non-destructive flaw detection,” *Smart Mater. Struct.*, vol. 2, no. 1, p. 22, 1993.

[16] D. D. L. Chung, “Cement reinforced with short carbon fibers: a multifunctional material,” *Compos. Part B Eng.*, vol. 31, no. 6–7, pp. 511–526, Oct. 2000.

[17] X. Fu and D. D. L. Chung, “Contact electrical resistivity between cement and carbon fiber: Its decrease with increasing bond strength and its increase during fiber pull-out,” *Cem. Concr. Res.*, vol. 25, no. 7, pp. 1391–1396, Oct. 1995.

[18] X. Yu and E. Kwon, “A carbon nanotube/cement composite with piezoresistive properties,” *Smart Mater. Struct.*, vol. 18, no. 5, p. 055010, 2009.

[19] F. J. Baeza, O. Galao, E. Zornoza, and P. Garcés, “Multifunctional Cement Composites Strain and Damage Sensors Applied on Reinforced Concrete (RC) Structural Elements,” *Materials*, vol. 6, no. 3, pp. 841–855, Mar. 2013.

[20] H. Li, H. Xiao, and J. Ou, “Effect of compressive strain on electrical resistivity of carbon black-filled cement-based composites,” *Cem. Concr. Compos.*, vol. 28, no. 9, pp. 824–828, Oct. 2006.

[21] D. D. L. Chung, “Piezoresistive Cement-Based Materials for Strain Sensing,” *J. Intell. Mater. Syst. Struct.*, vol. 13, no. 9, pp. 599–609, Sep. 2002.

[22] S. Das, B. Souliman, D. Stone, and N. Neithalath, “Synthesis and Properties of a Novel Structural Binder Utilizing the Chemistry of Iron Carbonation,” *ACS Appl. Mater. Interfaces*, vol. 6, no. 11, pp. 8295–8304, Jun. 2014.

[23] S. Das, D. Stone, D. Convey, and N. Neithalath, “Pore- and micro-structural characterization of a novel structural binder based on iron carbonation,” *Mater. Charact.*, vol. 98, pp. 168–179, Dec. 2014.

[24] S. Das, A. B. Kizilkanat, S. Chowdhury, D. Stone, and N. Neithalath, “Temperature-induced phase and microstructural transformations in a synthesized iron carbonate (siderite) complex,” *Mater. Des.*, vol. 92, pp. 189–199, Feb. 2016.

[25] R. Kumar, A. Thangaraj, R. N. Bhat, and P. Ratnasamy, “Synthesis of iron-silicate analogs of zeolite beta,” *Zeolites*, vol. 10, no. 2, pp. 85–89, Feb. 1990.

[26] N. Neithalath and J. Jain, “Relating rapid chloride transport parameters of concretes to microstructural features extracted from electrical impedance,” *Cem. Concr. Res.*, vol. 40, no. 7, pp. 1041–1051, Jul. 2010.

[27] S. Das, A. Kizilkanat, and N. Neithalath, “Crack propagation and strain localization in metallic particulate-reinforced cementitious mortars,” *Mater. Des.*, vol. 79, pp. 15–25, Aug. 2015.

[28] B. Díaz, L. Freire, P. Merino, X. R. Nóvoa, and M. C. Pérez, “Impedance spectroscopy study of saturated mortar samples,” *Electrochimica Acta*, vol. 53, no. 25, pp. 7549–7555, Oct. 2008.

[29] G. Song, “Equivalent circuit model for AC electrochemical impedance spectroscopy of concrete,” *Cem. Concr. Res.*, vol. 30, no. 11, pp. 1723–1730, Nov. 2000.

[30] W. J. McCarter and R. Brousseau, “The A.C. response of hardened cement paste,” *Cem. Concr. Res.*, vol. 20, no. 6, pp. 891–900, Nov. 1990.

[31] S. Das, B. Souliman, D. Stone, and N. Neithalath, “Synthesis and Properties of a Novel Structural Binder Utilizing the Chemistry of Iron Carbonation,” *ACS Appl. Mater. Interfaces*, vol. 6, no. 11, pp. 8295–8304, Jun. 2014.

[32] Jinping Ou and Baoguo Han, “Piezoresistive Cement-based Strain Sensors and Self-sensing Concrete Components,” *J. Intell. Mater. Syst. Struct.*, vol. 20, no. 3, pp. 329–336, Feb. 2009.

[33] R. M. C. Mimoso, J. M. da S. C. R. Pereira, and J. C. F. Pereira, “Computational Method for Calculating the Effective Permittivity of Complex Mixtures,” *J. Microw. Power Electromagn. Energy*, vol. 49, no. 2, pp. 85–99, Jan. 2015.

[34] S. K. Saha, “Nanodielectrics with giant permittivity,” *Bull. Mater. Sci.*, vol. 31, no. 3, pp. 473–477, Jun. 2008.

[35] C.-W. Nan, Y. Shen, and J. Ma, “Physical Properties of Composites Near Percolation,” *Annu. Rev. Mater. Res.*, vol. 40, no. 1, pp. 131–151, 2010.

[36] J. Peng, J. Yang, M. Huang, J. Sun, and Z. Wu, “Simulation and analysis of the effective permittivity for two-phase composite medium,” *Front. Mater. Sci. China*, vol. 3, no. 1, pp. 38–43, Mar. 2009.

[37] T. C. Choy, *Effective Medium Theory: Principles and Applications*. Clarendon Press, 1999.

[38] N. Yellepeddi, “Microstructural-Based Modeling of Electrical Percolation In Polymer Nanocomposites,” *Theses Diss.*, Jan. 2013.

[39] M. R. Raihan, “Dielectric Properties of Composite Materials during Damage Accumulation and Fracture,” *Theses Diss.*, Aug. 2014.

[40] P. M. Ajayan, “Nanotubes from Carbon,” *Chem. Rev.*, vol. 99, no. 7, pp. 1787–1800, Jul. 1999.

[41] B. I. Yakobson and R. E. Smalley, “Fullerene Nanotubes: C 1,000,000 and Beyond: Some unusual new molecules—long, hollow fibers with tantalizing electronic and mechanical properties—have joined diamonds and graphite in the carbon family,” *Am. Sci.*, vol. 85, no. 4, pp. 324–337, 1997.

[42] S. K. Bhattacharya and A. C. D. Chaklader, “Review on Metal-Filled Plastics. Part1. Electrical Conductivity,” *Polym.-Plast. Technol. Eng.*, vol. 19, no. 1, pp. 21–51, Jan. 1982.

[43] R. Font, O. Raymond, E. Martinez, J. Portelles, and J. M. Siqueiros, “Ferroelectric hysteresis and aging effect analysis in multiferroic Pb(Fe0.5Nb0.5)O3 ceramics,” *J. Appl. Phys.*, vol. 105, no. 11, p. 114110, Jun. 2009.

[44] K. S. Cole and R. H. Cole, “Dispersion and Absorption in Dielectrics I. Alternating Current Characteristics,” *J. Chem. Phys.*, vol. 9, no. 4, pp. 341–351, Apr. 1941.

[45] H.-Y. Wang, “Simulation And Evaluation Of Dielectric And Magnetoelectric Properties Of Diphasic And Layered Ferroic Composites,” Oct. 2008.

[46] A. Tarasov and K. Titov, “On the use of the Cole–Cole equations in spectral induced polarization,” *Geophys. J. Int.*, vol. 195, no. 1, pp. 352–356, Oct. 2013.

[47] A. Robert, “Dielectric permittivity of concrete between 50 Mhz and 1 Ghz and GPR measurements for building materials evaluation,” *J. Appl. Geophys.*, vol. 40, no. 1–3, pp. 89–94, Oct. 1998.

[48] R. B. Yang, S. D. Hsu, and C. K. Lin, “Frequency-dependent complex permittivity and permeability of iron-based powders in 2–18 GHz,” *J. Appl. Phys.*, vol. 105, no. 7, p. 07A527, Apr. 2009.

[49] Y. Nie, H. He, Z. Zhao, R. Gong, and H. Yu, “Preparation, surface modification and microwave characterization of magnetic iron fibers,” *J. Magn. Magn. Mater.*, vol. 306, no. 1, pp. 125–129, Nov. 2006.

[50] H.-W. Song, C.-H. Lee, and K. Y. Ann, “Factors influencing chloride transport in concrete structures exposed to marine environments,” *Cem. Concr. Compos.*, vol. 30, no. 2, pp. 113–121, Feb. 2008.

[51] D. Toker, D. Azulay, N. Shimoni, I. Balberg, and O. Millo, “Tunneling and percolation in metal-insulator composite materials,” *Phys. Rev. B*, vol. 68, no. 4, p. 041403, Jul. 2003.

[52] S. Mercier, A. Molinari, and M. El Mouden, “Thermal conductivity of composite material with coated inclusions: Applications to tetragonal array of spheroids,” *J. Appl. Phys.*, vol. 87, no. 7, pp. 3511–3519, Mar. 2000.

[53] P. J. M. Monteiro, J. C. Maso, and J. P. Ollivier, “The aggregate-mortar interface,” *Cem. Concr. Res.*, vol. 15, no. 6, pp. 953–958, Nov. 1985.

[54] W.-Z. Cai, S.-T. Tu, and J.-M. Gong, "A Physically Based Percolation Model of the Effective Electrical Conductivity of Particle Filled Composites," *J. Compos. Mater.*, vol. 40, no. 23, pp. 2131–2142, Dec. 2006.

[55] B. Sareni, L. Krähenbühl, A. Beroual, and C. Brosseau, "Effective dielectric constant of periodic composite materials," *J. Appl. Phys.*, vol. 80, no. 3, pp. 1688–1696, Aug. 1996.

[56] "Structural Mechanics Analyses -Finite Element Analysis Software Structural Mechanics Analyses." [Online]. Available: https://www.comsol.com/structural-mechanics-module. [Accessed: 12-May-2017].

[57] D. D. L. Chung, "Strain sensors based on the electrical resistance change accompanying the reversible pull-out of conducting short fibers in a less conducting matrix," *Smart Mater. Struct.*, vol. 4, no. 1, p. 59, 1995.

[58] J. Roesler, G. H. Paulino, K. Park, and C. Gaedicke, "Concrete fracture prediction using bilinear softening," *Cem. Concr. Compos.*, vol. 29, no. 4, pp. 300–312, Apr. 2007.

[59] A. Hillerborg, M. Modéer, and P.-E. Petersson, "Analysis of crack formation and crack growth in concrete by means of fracture mechanics and finite elements," *Cem. Concr. Res.*, vol. 6, no. 6, pp. 773–781, Nov. 1976.

[60] P.-E. Petersson, "Crack growth and development of fracture zones in plain concrete and similar materials," 1981.

[61] V. S. Gopalaratnam and S. P. Shah, "Softening Response of Plain Concrete in Direct Tension," *J. Proc.*, vol. 82, no. 3, pp. 310–323, May 1985.

[62] Z. P. Bažant, Q. Yu, and G. Zi, "Choice of standard fracture test for concrete and its statistical evaluation," *Int. J. Fract.*, vol. 118, no. 4, pp. 303–337, Dec. 2002.

[63] V. Slowik, J. M. Chandra Kishen, and V. E. Saouma, "Mixed mode fracture of cementitious bimaterial interfaces;: Part I: Experimental results," *Eng. Fract. Mech.*, vol. 60, no. 1, pp. 83–94, May 1998.

[64] M. Aguayo *et al.*, "The influence of microencapsulated phase change material (PCM) characteristics on the microstructure and strength of cementitious

composites: Experiments and finite element simulations," *Cem. Concr. Compos.*, vol. 73, pp. 29–41, Oct. 2016.

APPENDIX A

INTERFACE-BACK-CALCULATION MATLAB FORMULATION

```
clc;

clear all;
syms particle interface;
freq(:,1)= xlsread('dielectric_18sept.xlsx','OPC_input','A2:A72');
OPC(:,1)= xlsread('dielectric_18sept.xlsx','OPC_input','B2:B72');
composite(:,1)=xlsread('dielectric_18sept.xlsx','composite','B2:B72');
i=size(freq,1);
yf =zeros([i,1]);
cparticle=zeros([i,1]);
cinterface=zeros([2,i]);
s =zeros([1,2]);
%For circular inclusions
a=21; %micron
b=21; %micron
lamda = 5;% thickness of interface
% volume fraction of conductive particle
v = (a*b*b)/((a+lamda)*(b+lamda)*(b+lamda));
vf = 0.3;
vfe = (vf/v);
d=100;% conductivity of iron

for j=1:1:i
   y1 = (9-9*vfe)*((OPC(j,1)^1.14 - composite(j,1)^1.4)/(OPC(j,1)^1.14 +
2*composite(j,1)^1.4))+vfe*(((particle^0.5-
composite(j,1)^0.5)/(composite(j,1)+1/3*(particle^0.5-composite(j,1)^0.5))));
   y2 = vfe*(4*((particle^0.5-composite(j,1)^0.5)/(2*(composite(i,1))^0.5)*(1-
1/3)*(particle^0.5-composite(j,1)^0.5)));
   ys=solve(y1+y2==0,particle);
   cparticle(j,1)=vpa(ys(1,1));
end
% the variables are conductivity of iron, the thickness of ITZ(more
% conducting than OPC
% calculating the conductivity of effective particle using Wen ZHONG Chai et al.(2005)

for k=1:1:i
   eqn1=((3*(1-v))/interface)*(cparticle(k,1)-interface);
   eqn2=(v*(cparticle(k,1)-100)/(interface+(1/3)*(d-interface)));
   eqn3=( 4*v*(cparticle(k,1)-100)/((2*interface)+((1-(1/3))*(d-interface))));
   s=solve(eqn1+eqn2+eqn3==0,interface);
   cinterface(k,1:2)=vpa(s)
end;
```

APPENDIX B

BASIC MICROSTRUCTURAL FORMULATION FOR SOLID MECHANICS MODULE

```
clc
clear all
close all

%-------------------------------------------------------------------------------%
%Initial parameters
%-------------------------------------------------------------------------------%
dx = 200;                   % Domain range in x-direction
dy = 200;                   % Domain range in x-direction
dxx = 197;
dyy = 197;
r_min = 1;                  % minimum radius of void
r_max = 1;                  % maximum radius of void
Vol_Fractioni = 0.30;           % Volume fraction of voids
Vol_Fractionv = 0.01;
R_inclusion = 20;               % Radius of inclusion
R_interface = 25;
thickness =5;               % Thickness of interface

%=================================================================
====================%
% Void generation
%=================================================================
====================%
% Code beginning for first void generation
A = zeros(dx,dy);
S = dx*dy;
S_partical = 0;
ratio = S_partical/S;
count = 1;
R = r_max;
%*************************************************************************
%*****************Random inclusion generation************************
%*************************************************************************
X(count) = round((165-30)*rand(1)+30); %draw a single value form 1 to dx
Y(count) = round((165-30)*rand(1)+30);% Xcount is the centre of the circle
for xx=(X(count)-R_interface):(X(count)+R_interface)
   for yy = (Y(count)-R_interface):(Y(count)+R_interface)
      if (sqrt((xx-X(count))^2+(yy-Y(count))^2) <=R_interface)% eq of ellipse
         x = xx;
         y = yy;
         if y <= 0
            y =1;
         end
         if x <= 0
            x =1;
```

```
            end
            A(x,y)= 1;
        end
    end
end
Area = 0;
for i=1:dx
    for y=1:dy
        if (A(i,y) == 1)
            Area = Area + 1;
        end
    end
end
while(ratio<Vol_Fractioni)
    count = count+1;
    X(count) = round((165-30)*rand(1)+30); %draw a single value form 1 to dx
    Y(count) = round((165-30)*rand(1)+30);% Xcount is the centre of the circle
    i=1;
    while (i<=(count-1))
        dist(i) = sqrt((X(count)-X(i))^2+(Y(count)-Y(i))^2);% Checking the spacing
between two voids.xcoor count is new point and xcoor(i) is old
        length(i) = 6+(2*R_inclusion);
        if ((length(i)+1)>=dist(i))% threshold adjustment done here
          X(count) = round((165-30)*rand(1)+30); %draw a single value form 1 to dx
          Y(count) = round((165-30)*rand(1)+30);% Xcount is the centre of the circle
          i=1;
        else
            i=i+1;% this breaks the loops
        end
    end

    for xx=(X(count)-R_inclusion):(X(count)+R_inclusion)
        for yy = (Y(count)-R_inclusion):(Y(count)+R_inclusion)
            if sqrt((xx-X(count))^2+(yy-Y(count))^2)<=R_inclusion
                x = xx;
                y = yy;
                if y <= 0
                    y =1;
                end
                if x <= 0
                    x =1;
                end
                A(x,y)= 1;
            end
        end
    end
```

```
    Area = 0;
    for i=1:dx
        for y=1:dy
            if (A(i,y) == 1)
                Area = Area + 1;
            end
        end
    end
    ratio = Area/S
end

%*************************************************************************
%*****************Random void generation ***************************
%*************************************************************************

A = zeros(dx,dy);
for i=1:dxx
    for j =1:dyy
        for counter =1:count
            if ( (i-X(counter))^2+(j-Y(counter))^2)<(R_interface+5)^2
                A(i,j)=2;
            end
        end
    end
end
S = dx*dy;
S_partical = 0;
ratio = S_partical/S;
countv = 1;
R = r_max;
xcoorv(countv) = round((dxx-5)*rand(1)+5); %draw a single value form 1 to dx
ycoorv(countv) = round((dyy-5)*rand(1)+5);% Xcount is the centre of the circl
for counter =1:count
    if ((X(counter)-xcoorv(countv))^2+(Y(counter)-
ycoorv(countv))^2)<(R_interface+5)^2
        xcoorv(countv) = round((dxx-5)*rand(1)+5); %draw a single value form 1 to dx
        ycoorv(countv) = round((dyy-5)*rand(1)+5);% Xcount is the centre of the circl
    end
end
for xx=(xcoorv(countv)-R):(xcoorv(countv)+R)
    for yy = (ycoorv(countv)-R):(ycoorv(countv)+R)
        if (sqrt((xx-xcoorv(countv))^2+(yy-ycoorv(countv))^2)<=R)
            x = xx;
            y = yy;
            if y <= 0
                y =1;
```

```
            end
            if x <= 0
               x =1;
            end
            A(x,y)= 1;
         end
      end
   end
   Area = 0;
   for i=1:dx
      for y=1:dy
         if (A(i,y) == 1)
            Area = Area + 1;
         end
      end
   end

   while(ratio<Vol_Fractionv)
      countv = countv+1;
      xcoorv(countv) = round((dxx-5)*rand(1)+5);
      ycoorv(countv) = round((dyy-5)*rand(1)+5);
      i=1;
      while (i<=(countv-1))
         dist(i) = sqrt((xcoorv(countv)-xcoorv(i))^2+(ycoorv(countv)-ycoorv(i))^2);%
   Checking the spacing between two voids.xcoor count is new point and xcoor(i) is old
         length(i) = 2*R;
         z =A(xcoorv(countv),ycoorv(countv));
         if ((length(i)+1)>=dist(i)||z==2)% threshold adjustment done here
            xcoorv(countv) = round((dxx-5)*rand(1)+5); %draw a single value form 1 to dx
            ycoorv(countv) = round((dyy-5)*rand(1)+5);% Xcount is the centre of the circle
            i=1;
         else
            i=i+1;% this breaks the loops
         end
      end
      for xx=(xcoorv(countv)-R):(xcoorv(countv)+R)
         for yy = (ycoorv(countv)-R):(ycoorv(countv)+R)
            if (sqrt((xx-xcoorv(countv))^2+(yy-ycoorv(countv))^2)<=R)
               x = xx;
               y = yy;
               if y <= 0
                  y =1;
               end
               if x <= 0
                  x =1;
               end
```

```
            A(x,y)= 1;
        end
    end
end
Area = 0;
for i=1:dx
    for y=1:dy
        if (A(i,y) == 1)
            Area = Area + 1;
        end
    end
end
ratio = Area/S
end
%*****************************************************************
%***************COMSOL generation*****************************
%*****************************************************************

ParticalNum = count;
Pos = zeros (ParticalNum,2);
disp('****************************************')
disp('Microstructure generation starts now :)')
disp('****************************************')
for i=1:ParticalNum
    Pos(i,1)=X(i);
    Pos(i,2)=Y(i);
end
disp('Coordinates stored in Pos vector')


import com.comsol.model.*
import com.comsol.model.util.*

model = ModelUtil.create('Model');
geom1 = model.geom.create ('geom1',2);
sp_num = 2;
blk_length = dx;
blk_size = [blk_length,blk_length];
blk_position = [0 0];

%***********************For
interface*****************************************

model.geom('geom1').feature.create('interface1','Circle');% Creating circle2 with radius
30micron
```

```
model.geom('geom1').feature('interface1').set('r',R_interface);% Setting the radius to 30
micron
model.geom('geom1').feature('interface1').set('pos',[Pos(1,1) Pos(1,2)]); %  Setting the
position of 30 micron
model.geom('geom1').run('interface1')
sph_name_cell = {'interface1'};

for i=2:ParticalNum
   sph_name = strcat('interface',int2str(i));
   model.geom('geom1').feature.create(sph_name,'Circle');
   model.geom('geom1').feature(sph_name).set('r',R_interface);
   model.geom('geom1').feature(sph_name).set('pos',[Pos(i,1) Pos(i,2)]);
   model.geom('geom1').run(sph_name);
   sph_name_cell{i}=sph_name;
end

% Creating the domain of RVE

model.geom('geom1').feature.create('sqr','Rectangle');% creating a geometry
model.geom('geom1').feature('sqr').set('size',[dx dy]);% size of the square
model.geom('geom1').feature('sqr').set('pos',[0 0]); % position of the square

% Creating Union

model.geom('geom1').feature.create('uni1','Union');
model.geom('geom1').feature('uni1').selection('input').set({'interface1' 'sqr'});
model.geom('geom1').run('uni1');

for i=2:ParticalNum
   unions_old=strcat('uni',int2str(i-1));
   unions=strcat('uni',int2str(i));
   model.geom('geom1').feature.create(unions,'Union');
   model.geom('geom1').feature(unions).selection('input').set({unions_old
sph_name_cell{i}});
   model.geom('geom1').run(unions);
end

%**********************For inclusion to make
difference*******************************
model.geom('geom1').feature.create('inclusion1','Circle');% Creating circle2 with radius
30micron
model.geom('geom1').feature('inclusion1').set('r',R_inclusion);% Setting of the void
model.geom('geom1').feature('inclusion1').set('pos',[Pos(1,1) Pos(1,2)]); % Position of
first circle with 20 micron
model.geom('geom1').run('inclusion1') % to run the newly created sphere 1.
sph_name_celll={'inclusion1'};
```

```
for i=2:ParticalNum
    sph_namee = strcat('inclusion',int2str(i));
    model.geom('geom1').feature.create(sph_namee,'Circle');
    model.geom('geom1').feature(sph_namee).set('r',R_inclusion);
    model.geom('geom1').feature(sph_namee).set('pos',[Pos(i,1) Pos(i,2)]);
    model.geom('geom1').run(sph_namee);
    sph_name_celll{i}=sph_namee;
end

%**************Creating Difference************************

diff1=geom1.feature.create('diff1','Difference');
diff1.selection('input').set('uni9');
diff1.selection('input2').set('inclusion1');
model.geom('geom1').run('diff1');


for i=2:ParticalNum
    diff_old=strcat('diff',int2str(i-1));
    diff=strcat('diff',int2str(i));
    model.geom('geom1').feature.create(diff,'Difference');
    model.geom('geom1').feature(diff).selection('input').set(diff_old);
    model.geom('geom1').feature(diff).selection('input2').set( sph_name_celll{i});
    model.geom('geom1').run(diff);
end

%**********************Creating inclusion for
geometry*****************************

model.geom('geom1').feature.create('inclusioni1','Circle');% Creating circle2 with radius
30micron
model.geom('geom1').feature('inclusioni1').set('r',R_inclusion);% Setting of the void
model.geom('geom1').feature('inclusioni1').set('pos',[Pos(1,1) Pos(1,2)]); % Position of
first circle with 20 micron
model.geom('geom1').run('inclusioni1') % to run the newly created sphere 1.
sph_name_ceelll={'inclusioni1'};

for i=2:ParticalNum
    sph_nammee = strcat('inclusioni',int2str(i));
    model.geom('geom1').feature.create(sph_nammee,'Circle');
    model.geom('geom1').feature(sph_nammee).set('r',R_inclusion);
    model.geom('geom1').feature(sph_nammee).set('pos',[Pos(i,1) Pos(i,2)]);
    model.geom('geom1').run(sph_nammee);
    sph_name_ceelll{i}=sph_nammee;
end
```

```
%************************For voids
generation*********************************
ParticalNum = countv;
Pos = zeros (ParticalNum,2);
disp('*********************************************')
disp('This is the start of the program for voids...')
disp('*********************************************')
for i=1:ParticalNum
   Pos(i,1)=xcoorv(i);
   Pos(i,2)=ycoorv(i);
end
Num=0;

disp('Coordinates have been generated for voids...')
disp('=========================================')
disp('Start creating COMSOL geometry.....')

model.geom('geom1').feature.create('void1','Circle');
model.geom('geom1').feature('void1').set('r',R);% Setting R of voids for 1 micron
model.geom('geom1').feature('void1').set('pos',[Pos(1,1) Pos(1,2)]); % Position of first
circle with 20 micron
model.geom('geom1').run('void1') % to run the newly created sphere 1.

sph_name_ccell = {'void1'};

for i=2:ParticalNum

   sph_naame = strcat('void',int2str(i));
   model.geom('geom1').feature.create(sph_naame,'Circle');
   model.geom('geom1').feature(sph_naame).set('r',R);
   model.geom('geom1').feature(sph_naame).set('pos',[Pos(i,1) Pos(i,2)]);
   model.geom('geom1').run(sph_naame);
   sph_name_ccell{i}=sph_naame;
end

model.geom('geom1').runAll;
mphgeom(model,'geom1');
mphsave(model,'1%_voids_30%_inclusions_24April2017');
```

APPENDIX C

BASIC MICROSTRUCTURAL FORMULATION FOR ELECTRIC CURRENTS MODULE

```
clc;

clear all;
%-------------------------------------------------------------------------------%
%Initial parameters
%-------------------------------------------------------------------------------%
dx = 200;                   % Domain range in x-direction
dy = 200;                   % Domain range in x-direction
dxx = 197;
dyy = 197;
r_min = 1;                  % minimum radius of void
r_max = 1;                  % maximum radius of void
Vol_Fractioni = 0.20;           % Volume fraction of voids
Vol_Fractionv = 0.01;
R_inclusion = 20;               % Radius of inclusion
R_interface = 25;
thickness =5;               % Thickness of interface
R = r_max;
%*******************************************************************************
*****************
%*****************************parameters for
coordinates************************************
%*******************************************************************************
*****************

ParticalNum = 9;
VoidNum=80;
Pos = zeros (ParticalNum,2);
for i=1:ParticalNum
   Pos(:,1)= xlsread('location.xlsx','1%_30%','B4:J4');
   Pos(:,2)= xlsread('location.xlsx','1%_30%','B5:J5');
end

for i=1:VoidNum
   Posv(:,1)= xlsread('location.xlsx','1%_30%','B1:CC1');
   Posv(:,2)= xlsread('location.xlsx','1%_30%','B2:CC2');
end

disp('****************************************')
disp('Microstructure generation starts now :)')
disp('****************************************')

import com.comsol.model.*
import com.comsol.model.util.*

model = ModelUtil.create('Model');
```

```
geom1 = model.geom.create ('geom1',2);
sp_num = 2;
blk_length = dx;
blk_size = [blk_length,blk_length];
blk_position = [0 0];

%**********For
interface**************************************

model.geom('geom1').feature.create('interface1','Circle');% Creating circle2 with radius
30micron
model.geom('geom1').feature('interface1').set('r',R_interface);% Setting the radius to 30
micron
model.geom('geom1').feature('interface1').set('pos',[Pos(1,1) Pos(1,2)]); %  Setting the
position of 30 micron
model.geom('geom1').run('interface1')
sph_name_cell = {'interface1'};

for i=2:ParticalNum
    sph_name = strcat('interface',int2str(i));
    model.geom('geom1').feature.create(sph_name,'Circle');
    model.geom('geom1').feature(sph_name).set('r',R_interface);
    model.geom('geom1').feature(sph_name).set('pos',[Pos(i,1) Pos(i,2)]);
    model.geom('geom1').run(sph_name);
    sph_name_cell{i}=sph_name;
end

% Creating the domain of RVE

model.geom('geom1').feature.create('sqr','Rectangle');% creating a geometry
model.geom('geom1').feature('sqr').set('size',[dx dy]);% size of the square
model.geom('geom1').feature('sqr').set('pos',[0 0]); % position of the square

%**********For inclusion ******************************
model.geom('geom1').feature.create('inclusion1','Circle');% Creating circle2 with radius
30micron
model.geom('geom1').feature('inclusion1').set('r',R_inclusion);% Setting of the void
model.geom('geom1').feature('inclusion1').set('pos',[Pos(1,1) Pos(1,2)]); % Position of
first circle with 20 micron
model.geom('geom1').run('inclusion1') % to run the newly created sphere 1.
sph_name_celll={'inclusion1'};

for i=2:ParticalNum
    sph_namee = strcat('inclusion',int2str(i));
    model.geom('geom1').feature.create(sph_namee,'Circle');
    model.geom('geom1').feature(sph_namee).set('r',R_inclusion);
```

```
    model.geom('geom1').feature(sph_namee).set('pos',[Pos(i,1) Pos(i,2)]);
    model.geom('geom1').run(sph_namee);
    sph_name_celll{i}=sph_namee;
end

%**********For debonding@top**************************************
model.geom('geom1').feature.create('debonding','Ellipse');% Creating circle2 with radius 30micron
model.geom('geom1').feature('debonding').set('semiaxes',[5 0.003]);% Setting the radius to 30 micron
model.geom('geom1').feature('debonding').set('pos',[Pos(1,1) Pos(1,2)+20.0015]); % Setting the position of 30 micron
model.geom('geom1').run('debonding')
sph_namee_cell = {'debonding'};

for i=2:ParticalNum
    sph_namee = strcat('debond',int2str(i));
    model.geom('geom1').feature.create(sph_namee,'Ellipse');
    model.geom('geom1').feature(sph_namee).set('semiaxes',[5 0.003]);
    model.geom('geom1').feature(sph_namee).set('pos',[Pos(i,1) Pos(i,2)+20.0015]);
    model.geom('geom1').run(sph_namee);

    sph_namee_cell{i}=sph_namee;

end

%**********For debonding@bottom**************************************
model.geom('geom1').feature.create('debondingb','Ellipse');% Creating circle2 with radius 30micron
model.geom('geom1').feature('debondingb').set('semiaxes',[5 0.003]);% Setting the radius to 30 micron
model.geom('geom1').feature('debondingb').set('pos',[Pos(1,1) Pos(1,2)-20.0015]); % Setting the position of 30 micron
model.geom('geom1').run('debondingb')
sph_naame_cell = {'debondingb'};

for i=2:ParticalNum

    sph_naame = strcat('debondb',int2str(i));
    model.geom('geom1').feature.create(sph_naame,'Ellipse');
    model.geom('geom1').feature(sph_naame).set('semiaxes',[5 0.003]);
    model.geom('geom1').feature(sph_naame).set('pos',[Pos(i,1) Pos(i,2)-20.0015]);
    model.geom('geom1').run(sph_naame);
```

```
    sph_naame_cell{i}=sph_naame;

end


%************************For voids
generation*********************************

model.geom('geom1').feature.create('void1','Circle');
model.geom('geom1').feature('void1').set('r',R);% Setting R of voids for 1 micron
model.geom('geom1').feature('void1').set('pos',[Posv(1,1) Posv(1,2)]); % Position of first
circle with 20 micron
model.geom('geom1').run('void1') % to run the newly created sphere 1.

sph_name_ccell = {'void1'};

for i=2:VoidNum

    sph_naame = strcat('void',int2str(i));
    model.geom('geom1').feature.create(sph_naame,'Circle');
    model.geom('geom1').feature(sph_naame).set('r',R);
    model.geom('geom1').feature(sph_naame).set('pos',[Posv(i,1) Posv(i,2)]);
    model.geom('geom1').run(sph_naame);
    sph_name_ccell{i}=sph_naame;
end


model.geom('geom1').runAll;
mphgeom(model,'geom1');
mphsave(model,'30%_electrical_5_2');
```